iScience

CellPress
OPEN ACCESS

Article

Diffusion-Controlled Porous Crystalline Silicon Lithium Metal Batteries

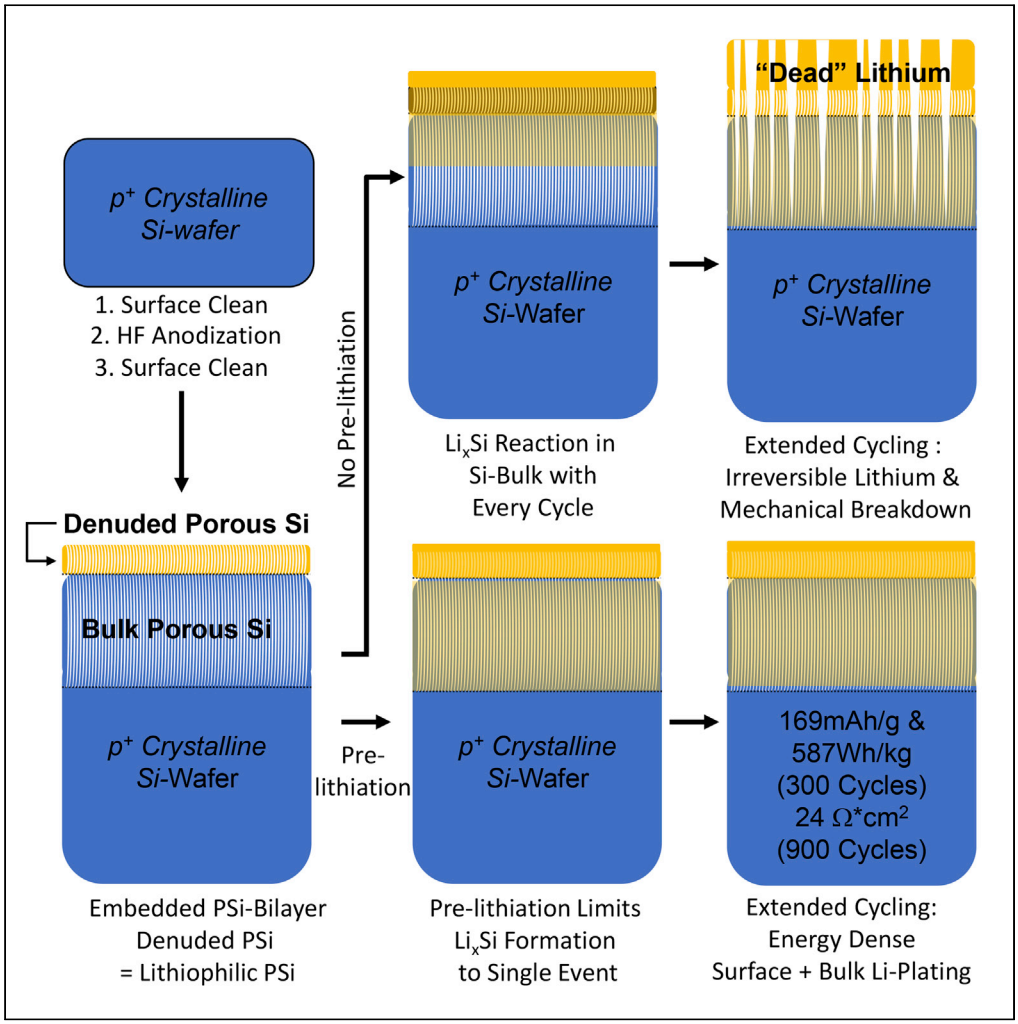

John Collins, Joel P. de Souza, Marinus Hopstaken, John A. Ott, Stephen W. Bedell, Devendra K. Sadana

3dsurfacechem@gmail.com (J.C.)
dsadana@us.ibm.com (D.K.S.)

HIGHLIGHTS

Porous crystalline silicon (PCS) anodes were seamlessly integrated in silicon wafers

A diffusion-controlling lithiophilic anode surface was created during fabrication

Full cells delivered energy dense performance: 169mAh/g, 587 Wh/kg for 300 cycles

Non-hazardous, pure silicon Li-metal-host anodes at industry-pace throughput

Collins et al., iScience 23, 101586
October 23, 2020
https://doi.org/10.1016/j.isci.2020.101586

iScience

CellPress
OPEN ACCESS

Article

Diffusion-Controlled Porous Crystalline Silicon Lithium Metal Batteries

John Collins,[1,2,3,*] Joel P. de Souza,[1,2] Marinus Hopstaken,[1] John A. Ott,[1] Stephen W. Bedell,[1] and Devendra K. Sadana[1,*]

SUMMARY

Nanostructured porous silicon materials have recently advanced as hosts for Li-metal plating. However, limitations involve detrimental silicon self-pulverization, Li-dendrites, and the ability to achieve wafer-level integration of non-composite, pure silicon anodes. compo. Herein, full cells featuring low-resistance, wafer-scale porous crystalline silicon (PCS) anodes are embedded with a nanoporous Li-plating and diffusion-regulating surface layer upon combined wafer surface cleaning (SC) and anodization. LL Lithiophilic surface formation is illustrated via correlation of surface groups and X-ray structure. Low-cost SC-PCS anodes require no composite formulation, and pre-lithiation enables sustainable Li-metal plating/stripping on the lithiophilic surface and in SC-PCS bulk nanostructure. Anodization time and C-rate determined competitive full cell performance: NMC811 | 4800 s SC-PCS: 195 mAh/g (99.9% coulombic efficiency [C.E.], C/3, 50 cycles), 165 mAh/g, 587 Wh/kg (97.1% C.E., C/3 and C/2 rate, 350 cycles), 24 Ω*cm^2 SC-PCS-resistivity (900 cycles); 160 μm LCO | 500 s SC-PCS: 102 mAh/g (94.1% C.E., 1C, 350 cycles).

INTRODUCTION

Lithium ion batteries are the energy storage medium of choice for mobile devices of all scales—from Internet of Things applications to electric vehicles. Due to its theoretically high energy density (12 kWh/kg), specific capacity (3,860 mAh/g), and the lowest reduction potential (−3.04V), lithium metal anodes are experiencing an innovative resurgence. Commercial lithium metal anodes are especially feasible with the advent of nonflammable, fluorinated, or in-cell protective elements (Chen et al., 2020; Collins et al., 2020b; Cui et al., 2020; Fan et al., 2018; Han et al., 2017; Liu et al., 2020); the advancement of solid electrolytes; custom solid-electrolyte interphase (SEI); and solid-electrolyte composites (Athanasiou et al., 2020a, 2020b; Fu et al., 2019; Harry et al., 2014; Tsai et al., 2016; Wu et al., 2018), which can effectively prevent hazardous Li-dendrite formation and support sustainable Li-plating processes. Another Li-metal anode approach relies on the creation of 2D or 3D electrodes that are able to suppress Li-dendrites through specific architecture and/or inherent energetic properties as a Li-metal host (Jiao et al., 2018; Yan et al., 2016; Yang et al., 2015; Zhou et al., 2018). A current leading material for the battery's anode is silicon (An et al., 2019; Hu et al., 2008; Ikonen et al., 2017) with a low cost (Jin et al., 2017; Kumagai, 2020) and high specific capacity (3,580–4,200 mAh/g) roughly 10 times that of commonly used graphite (~372 mAh/g). The use of silicon as a substrate for lithium-silicon alloying and/or lithium metal plating is a fast advancing field in anode materials development (Chen et al., 2019; Guo et al., 2010; Su et al., 2014). An often overlooked advantage of silicon as an active material is its suitability for high-throughput manufacturing and device integration of silicon wafer-level batteries (Collins et al., 2020a, 2020c; 2020d, 2020e; 2019; Gardner et al., 2016; Hahn et al., 2014; Hoeppner et al., 2015; Kumagai, 2020; Pikul and Ning, 2018) via world-wide existing semiconductor and microfabrication infrastructure (Collins et al., 2020e; Souza et al., 2020b, 2020a, 2020c).

Silicon can mechanically change in volume >400% upon incorporation of lithium, producing high-resistance mechanical separation and detrimental self-pulverization during cell cycling. To circumvent this, composite materials including high-surface-area porous carbon (Collins, 2014; Collins et al., 2018, 2015; 2014, 2013; Ferrari and Robertson, 2000), core-shell-type powder or slurry silicon additives (Chae et al., 2020; Guo et al., 2017; Hu et al., 2008; Jia et al., 2018; Vrankovic et al., 2017; Wang et al., 2013; Xing

[1]IBM T.J. Watson Research Center, 1101 Kitchawan Road, Rt 134, Yorktown Heights, New York 10598, USA

[2]These authors contributed equally

[3]Lead Contact

*Correspondence: 3dsurfacechem@gmail.com (J.C.), dsadana@us.ibm.com (D.K.S.)

https://doi.org/10.1016/j.isci.2020.101586

et al., 2018; Xu et al., 2018; Zhai et al., 2017), or porous silicon (PS) (An et al., 2019; Chen et al., 2019; Gardner et al., 2016; Ikonen et al., 2017; Jia et al., 2018; Karbassian, 2018; Lu et al., 2015b; Xiao et al., 2015) have been in constant development. PS-based systems, in particular, yield opportunities for advanced control of Li-diffusion and plating processes through the manipulation of internal silicon-charge dynamics, where crystal structure can be formidably tuned by select surface functional groups (Buttard et al., 1996; Ghannam et al., 2008; Sugiyama and Nittono, 1990) enabling enhancement of reversible electrochemical processes. Such surface-to-bulk structure/function relationships have been well elucidated via functional groups on high-surface-area carbon (Collins, 2014; Collins et al., 2018, 2015, 2014, 2013), thereby presenting an even greater opportunity for desired electrode performance when utilizing silicon with an additional filled π-orbital within Group 14 of the periodic table.

To further address self-pulverization and to harness the energy density of lithium metal, the use of silicon as a host material for lithium metal plating and stripping is currently being developed (Kumagai, 2020; Liang et al., 2016; Liu et al., 2017; Pender et al., 2020). Chen et al. (2019) illustrate the use of PS/NMC full cells using a PS-carbon binder composite anode. The composite anode enables high coulombic efficiency (>99.7%) for 300 cycles by suppressing the formation of "dead lithium" due to the higher delithiation potential of Li_xSi compared with Li-metal stripping—thereby enabling complete Li-metal stripping (of surface and Si-bulk plated Li-metal) before deleterious Li_xSi delithiation. Tang et al. (2018) utilize silicon sputtering on lithium metal to create a homogeneous surface for sustainable Li-metal plating and dendrite prevention. Liang et al. (2016) utilize a 3D porous carbon-based "lithiophilic" coating resulting in a passivated, non-polar pore confined composite electrode that enables 3 mA/cm^2 for over 80 cycles. These promising advances use surface materials and coatings to anchor Li-metal (e.g., to a host), resulting in highly sustainable, dendrite-suppressed Li-metal plating/stripping processes with stable SEI layers (Zhang et al., 2018).

Electrochemical anodization with hydrofluoric acid (HF) also produces PS anodes and is more compatible with standard semiconductor processing. The technique opens the door to wafer-integrated PS without any powder or composite formulation, binders, or conductivity-enhancing additives (Gardner et al., 2016; Ikonen et al., 2017; Stragier et al., 2010; Unagami, 1980; Zhang et al., 2019). Recently, the seamless integration of porous crystalline silicon (PCS) into high boron-doped p+ silicon wafers has been demonstrated (Collins et al., 2020e; Souza et al., 2020b, 2020a, 2020c, 2020d). Similar to previous descriptions in the analogous etching of porous carbon systems (Collins et al., 2014, 2013), organic cleaning of substrates *before* or *during* porous-etching treatment, removes surface-passivating heteromaterial, alters the electrochemical accessibility of electrolyte and reactants, and consequentially manipulates internal π-bond density and surface defect composition of porous systems. This cleaning and select activation of surface functional groups enables tuning of the resulting pore properties and crystallite size to elicit desired Li-diffusion and surface chemistries (Collins, 2014; Collins et al., 2014). Sun et al. (2014) use HF etching (without surface cleaning [SC]) to modulate the ratio of non-polar, lithiophilic (Liang et al., 2016; Zhang et al., 2018) Si-H bonds versus polar Si-O groups. The interdependence of these surface bond types on compressive or tensile pore-stress was shown to directly determine silicon crystallinity, lattice distortions, and the degree of Si-Si bond breaking.

Recently, we have shown that when anodization is preceded by organic standard SC of the silicon substrate before etching, along with an additional SC after etching, the anodization process embeds a protective or "lithiophilic" (Liang et al., 2016; Zhang et al., 2018) interface on the silicon surface (Collins et al., 2020e; Souza et al., 2020a, 2020c; 2020d; Souza et al., 2020e). SC removes a majority of oxygen defect groups and replaces them with Si-H-terminated bonds, which produce an electrochemically protective lithiophilic nanoporous electrode, where the alteration of Si-O/Si-H surface functionality additionally increases the Si-Si crystallinity (Ghannam et al., 2008; Sun et al., 2014), compared with non-surface cleaned silicon wafer. Electrochemical anodization with surface cleaned p+ silicon wafers, therefore, has the potential to enable lithiophilic SC-PCS without any separation between porous and crystalline wafer components while seamlessly integrating the SC-PCS into patterned or planar wafer-level silicon (Collins et al., 2020e; Souza et al., 2020a; Souza et al., 2020e).

To our knowledge, this is the first report of a wafer-integrated SC-PCS anode containing a lithiophilic porous surface layer produced in a semiconductor industry-compatible method. In addition, pre-lithiated full cells featuring this SC-PCS anode were shown to be highly electrochemically functional. The simple organic SC, HF anodization, and pre-lithiation steps produce an embedded robust and protective porous

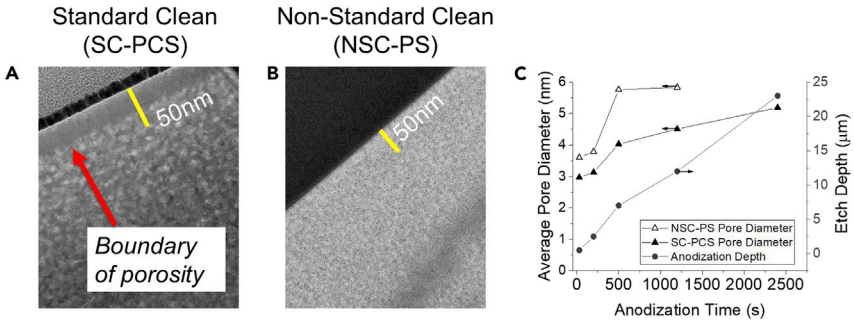

Figure 1. The Impact of Surface Cleaning on the Top Porous Surface Layer of Porous Silicon-Integrated Substrates

(A and B) TEM of silicon substrates (A) with pre/post-anodization standard cleaning (SC) and 200 s anodization time showing two porous layers and (B) non-surface cleaning (NSC) and 200 s anodization time showing only a single porous layer.

(C) Plot of average pore size and etch depth for various anodization times. Feature dimensions are illustrated with scale bars.

passivation layer with high crystallinity and low strain, which together regulate synchronous SC-PCS surface plating and bulk Li^+ diffusion to permit low-resistance, energy-dense long-term cycling. The SC-PCS electrode is able to sustain thousands of cycles while simultaneously preventing the growth of Li-dendrites as well as any detrimental volume or mechanical degradation, without the use of additives, SEI manipulation, or composite formulation.

RESULTS AND DISCUSSION

Dependence of Pore Physical Properties with Anodization Time and Surface Cleaning

Silicon wafers were etched for various durations in concentrated HF. The etching created well-defined porosity in the silicon wafer, where longer etch times resulted in a deeper porous layer and wider average pore sizes (Figures S1 and S2). Close examination by transmission electron microscopy (TEM) showed that in surface cleaned porous crystalline silicon (SC-PCS), see Transparent Methods, two porous layers result from etching—with a thinner (~30 nm) layer of smaller-diameter pores contained in the top porous crystalline region (Figure 1A). In non-surface cleaned porous silicon (NSC-PS), see Transparent Methods, there was only one PS layer integrated into the silicon wafer (Figure 1B). The average pore size ranged from approximately 3.0–5 nm for SC-PCS and 3.5–6 nm for NSC-PS (Figure 1C). On average, the SC pre/post-anodization treatment decreases the pore diameter of the top porous region by 1–2 nm, as determined by high magnification top-down scanning electron microscopic (SEM) averaging (Figure S2), where the top porous layer enables the extension of the decreased pore into the SC-PCS bulk (Figure S3).

SC-PCS anodes present uniquely high Si-Si crystallinity upon pore formation within the silicon wafer bulk, as evidenced by X-ray results (see Transparent Methods) from progressively anodized SC-PCS anodes. Figure 2 displays the associated X-ray diffraction (XRD) spectra for three progressively anodized SC-PCS samples for the (004) rocking curve peak region (Fahlman Bradley and Ramírez-Porras, 2012; Stragier et al., 2010). Figure 2A shows the relative angle versus intensity for 30, 200, and 1,200 s anodization times—displaying shifts in both relative angle and intensity as the anodization time is increased.

As the wafer-integrated SC-PCS layer becomes thicker with anodization time, the SC-PCS peak intensity and full width at half maximum increase, while a sharp peak profile is maintained—indicating an increase in the porosity size gradient, with uniform lattice expansion. The plateauing slope of the SC-PCS relative angle upon increased anodization time (Figure 2B), combined with the observed higher intensity and sharp peak features upon pore-gradient development (Figure 2A), is a result of stress-reduced PS formation (Sun et al., 2014).

Ghannam et al. (2008) were able to illustrate that the physical properties of Si-porosity strongly depend on the initial residual stress of the film, where the residual stress is directly related to both the initial pore radius and lateral strain acting on the surface of pores. Furthermore, the authors showed strain to be directly proportional to the presence of Si-adsorbed hydrogen—due to hydrogen's ability to prevent the

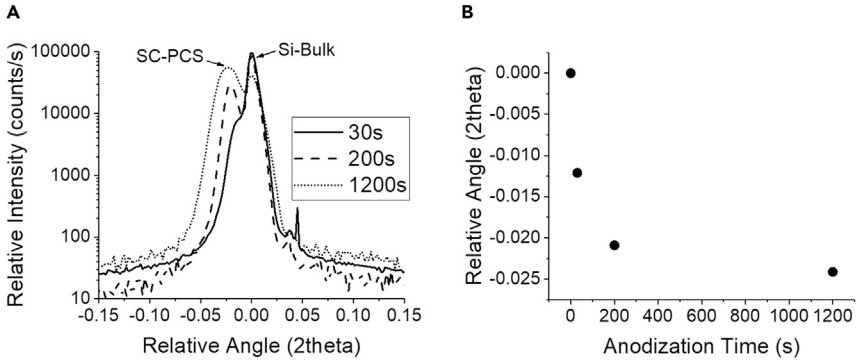

Figure 2. The XRD Rocking Curve Measurements for SC-PCS Samples the (004) Si Peak with Progressive Anodization Time

(A) 30 s, 200 s, and 1,200 s anodization time X-ray spectra.

(B) Relative angles of SC-PCS with anodization time.

rearrangement of Si-Si bonds during thermal treatment—and that lateral strain can be modified in proportion with surface-adsorbed hydrogen.

Table 1 shows the high Si-density, low porosity %, and low strain, as calculated from XRD spectra above and corresponding X-ray reflectivity (XRR) data (see Transparent Methods). The table illustrates the ability of the dense, highly crystalline denuded layer to create highly compact, crystalline nano-porosity within the bulk silicon upon anodization resulting from an inherent low strain, which is up to two orders of magnitude smaller, compared with similar reports of Si-etching (Buttard et al., 1999, 1996; Kim et al., 1991; Marty et al., 2006; Stragier et al., 2010; Sun et al., 2014).

Hence, just as Ghannam et al. (2008) illustrated by showing how the initial residual stress of the Si-film determines the ensuing pore-structure; herein, the top Si-surface porous layer (the denuded SC-PCS) maintains low residual stress, which permeates throughout the entire substrate during the anodization process, thereby resulting in a bulk structure with low-strain, highly compact PS. The low strain properties from the denuded layer translated into the silicon wafer result in well-defined, highly crystalline, and smaller nano-porosity deep within the silicon bulk (Figure S3), confirming the permeation of the denuded layer's structure properties throughout the substrate upon anodization.

Nanostructure and Molecular Analysis: Formation of Denuded Surface

Raman spectroscopy was used to examine the effect of SC and anodization on surface functionality to assess the impact of specific surface groups on SC-PCS crystallinity and pore properties. Figure 3 displays the Si-H_x vibration modes (Job et al., 2003; Ogata et al., 1995) of -$OSiH_3$ (~2,080cm^{-1}), -O_2SiH_2 (2105cm^{-1}), and O_3SiH (2135cm^{-1}) for the NSC-PS and SC-PCS anodized samples, shown in Figures 3A and 3B, respectively. The Raman spectra were deconvoluted for the specific vibration bands contained in the NSC-PS (Figure S4A) and SC-PCS (Figure S4B), with the peak intensities for different etch times compiled in Figure 3C. Compared with NSC, SC shows suppression of the primary surface -O_xSi—H_y vibration modes through lower associated peak intensities. SC treatment results in a significant loss of these -O_xSi—H_y bond types, and consequently a decrease in the concentration of O-Si crystalline defect sites.

NPH_x bonding (nanopore residing Si—H_x bonds) have previously been described by Job et al. (2003) as "somewhat disturbed vibrations of the Si-H_i modes (i = 1, 2, 3) of the hydrogen passivated internal surfaces of very small (nano-) voids/platelets." These bond alternations are most likely due to the highly constrained space inside NPH_x pores, where densely packed Si-H_x bonds now physically interact with neighboring bonds to a higher degree, shown as physiochemical-induced broad, convoluted Raman signals (Figures S4A and S4B). Notably, the concentration of ≲5-nm-diameter nanopore residing NPH_x intensity is very similar in magnitude for both the SC-PCS and NSC-PS anodes (Figure 4C; star symbols), yet SC-PCS samples contain a fraction of -O_xSi—H_y bond defects compared with NSC-PS samples for all anodization times.

Anodization Time (s)	Density (g/cm^3)	Porosity (%)	Strain (10^{-6})
0	2.33	0.0	0
30	2.09	10.3	220
200	1.86	20.2	295
1,200	1.63	30.0	341

Table 1. The Impact on Physical Properties of Standard Cleaned Porous Crystalline Silicon (SC-PCS) with Anodization Time

High concentrations of surface adsorbed hydrogen relieve tensile stress (Sun et al., 2014), passivate against further surface oxidation (Buttard et al., 1996; Sugiyama and Nittono, 1990), and reduce associated strain by preventing lattice distortion or rearrangement of crystalline Si-Si bonds on the developing porous system (Ghannam et al., 2008)—consequently enabling the highly crystalline, smaller nanoporosity of the denuded bearing SC-PCS. The removal of oxygen-containing heteromaterial during standard cleaning as shown with the Raman results from Figure 3 directly enables the low-strain, highly crystalline SC-PCS observed above with XRD (Figure 2). Concertedly, both lattice distortions and Si-Si bond breaking are suppressed, in seeming proportion with the removal of $O_xSi—H_y$ surface groups and the increased $NPH_x/O_xSi—H_y$ surface group ratio (Figure 3D). Statistically, higher $O_xSi—H_y$ surface group formation occurs with increased anodization time for both SC-PCS and NSC-PCS, yet at a far lower rate for SC-PCS compared with NSC-PCS. O_3Si_H groups were chosen as the NPH_x normalization factor (ratio denominator) as this species has been shown to dominate the surface of PS structures in hydrothermal or progressively oxidized environments (Jarvis et al., 2008; Ogata et al., 1995). Thus, the increasing slope (1.2) of SC-PCS's ratio rate shows that NPH_x can successfully persist, while O_3Si_H concentration increase is minimal with anodization time, where NSC-PS displays the opposite trend in group concentration and therefore a negative ratio slope (-2.9×10^{-5}) (Jarvis et al., 2008; Job et al., 2003; Ogata et al., 1995). The highly NPH_x-concentrated smaller pores are critical for increasing lithiophilic (lithium favoring) properties of the anode, as the non-polar surface groups facilitate non-reactive, sustainable Li-mobile and plating processes. The smaller, more lithiophilic pores are lined with non-reactive $Si-H_x$ bonds and fewer water-adsorbing Si-oxide (Jarvis et al., 2008) surface species (Figure 3A; arrow), which further supports lithiophilic character via sustainable plating and diffusion mobility by Li-species in organic electrolytes (Collins, 2014; Liang et al., 2016). Figure S4C shows that the relatively higher rate of $NPH_x/O_xSi—H_y$ surface group concentration with etch time enables shorter, stronger $-O_3Si_H$ (blue shifted) bond vibrations—confirming an increase in π-bond density at the surface edge, resulting from increased porosity and (albeit, at a low rate) surface oxygen group (SOG) formation (Collins et al., 2014, 2013). The pore size/SOG peak intensity and bond strength relationship show that SC-PCS substrates can maintain sustainable high crystalline Si-Si nanopores, at high oxidation times, even with significant electron delocalization from the silicon bulk via surface-site polarization. Only the SC-PCS substrates display the relatively high concentration of lithophilic Si-H-terminated nanopores that enable the highly crystalline Si-Si nanopore and Si-back-bonding structure (Jarvis et al., 2008; Job et al., 2003; Ogata et al., 1995).

The higher crystallinity and polarization-induced strain decrease from the combined increase of NPH_x surface groups and removal of $O_xSi—H_y$ surface groups in SC-PCS samples is further evidenced by the relative Si-Si bonding intensity, observed via Raman, for both SC and NSC sample sets (Figure S5). Si-Si bond intensity is known to develop upon progressive hydrogenation of amorphous silicon (Volodin and Koshelev, 2013). The intense Si-Si bonding is stable for progressive SC-PCS anodization times shown up to 2,400 s. Comparatively, NSC-PS samples (Figure S5B) display an initial increase (up to 500 s anodization time) in Si-Si peak intensity, most likely due to surface functional group electron-withdrawing effects experienced only during low oxidation times (Collins et al., 2013; Fahlman Bradley and Ramírez-Porras, 2012). NSC-PS samples show a decrease in Si-Si bond intensity after only 1,200 s of anodization time, illustrating a significant breakdown of silicon crystallinity from the high strain and Si-Si bond breaking resulting from the increased concentration of $O_xSi—H_y$ surface groups. SC-PCS samples present far more intense Si-Si Raman peaks at all etch times, whereas at increased oxidation times, NSC-PS samples display a decrease in Si-Si peak intensity due to the lack of densely packed NPH_x bonding resulting from increased surface oxide concentration—creating non-crystalline Si-lattice

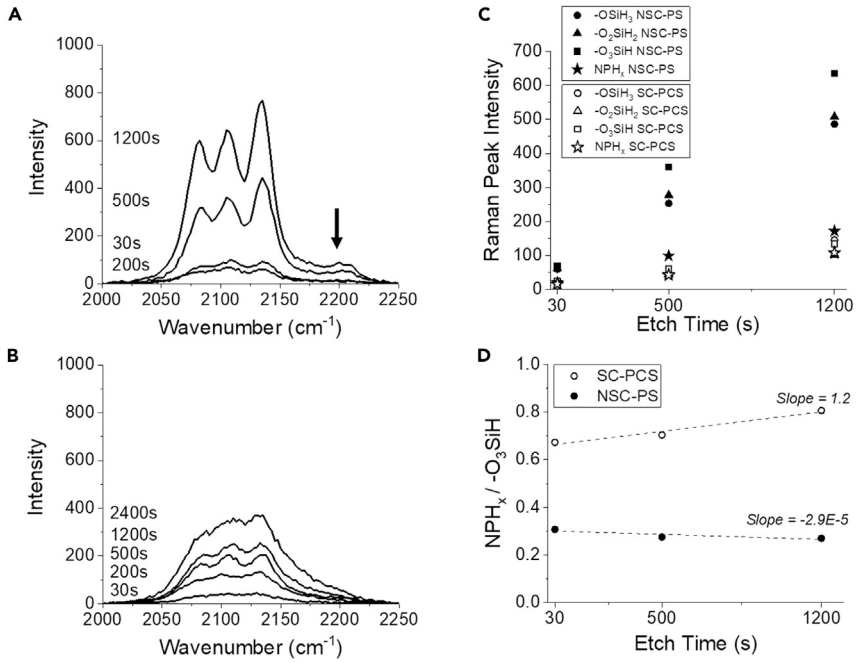

Figure 3. The Impact of Organic Particulate Cleaning on -O_xSi—H_y and Nanopore Si—H_x (NPH_x) Bond Formation in Non-Standard Porous Silicon (NSC-PS) and Standard Cleaned Porous Crystalline Silicon (SC-PCS) Substrates

(A and B) Raman -O_xSi—H_y vibration bands of (A) NSC-PS and (B) SC-PCS with increasing anodization times.

(C) Raman peak intensities from -$OSiH_3$, -O_2SiH_2, O_3SiH, and NPH_x deconvoluted vibration modes, shown in Figures S4A and S4B, for selected etch times.

(D) The ratio of O_3SiH to NPH_x peak intensities for SC-PCS and NSC-PS substrates with increasing etch times. Linear regression best fit slopes are displayed for both SC -PS and NSC-PS data.

alterations (Lee et al., 2005), a crystallite size reducing polarization effect (Collins et al., 2014), and Si-Si bond breaking at higher anodization times.

Non-pre-lithiated Denuded Porous Crystalline Silicon

Li-ion battery full cells were made using SC-PCS with 200 s HF anodized silicon anodes. TEM, SEM, and dynamic SIMs were used to examine the anodes in both a pre-cycled state and after 5 charge/discharge cycles (Figure 4). Pre-cycling, the battery shows enhanced crystalline, denuded porous region in the top ~30 nm of the silicon substrate, as described previously (Figure 4A). Further, the depth profile elemental analysis shows the removal of hydrogen, carbon, oxygen, and fluorine in the denuded region (Figure 3B), whereas the silicon concentration remains high—thereby reaffirming that the removal of heteromaterial, including precursor oxygen, which may result in the formation of the Si-Si bond breaking O_xSi—H_y surface groups discussed above.

After 5 charge/discharge cycles, the SEM cross section of the SC-PCS anode (Figure 4C) reveals a 2,700-nm-thick porous region + lithiated region, composed of (from top to bottom) a newly formed 50-nm SEI layer, a 220-nm plated lithium metal layer, followed by the original ~30-nm denuded silicon region. Upon cycling, a denser concentration of Li-metal space-fill and silicon compose the denuded SC-PCS layer, where the approximate denuded layer region is denoted by the dashed lines in Figure 4D. In addition, the denuded layer volume contains a constant, high concentration of hydrogen, whereas oxygen concentration drops significantly—thereby validating the NPH_x/O_xSi—H_y surface group-dependent lithiophilic character of the denuded layer, as discussed in previous sections. Deeper into the SC-PCS bulk, below the denuded layer, hydrogen and silicon concentration is high, whereas oxygen concentration remains low, yet it follows a parallel depth-concentration trend with lithium—indicating the formation of, e.g., Li_2O upon air exposure of the cross-sectioned sample.

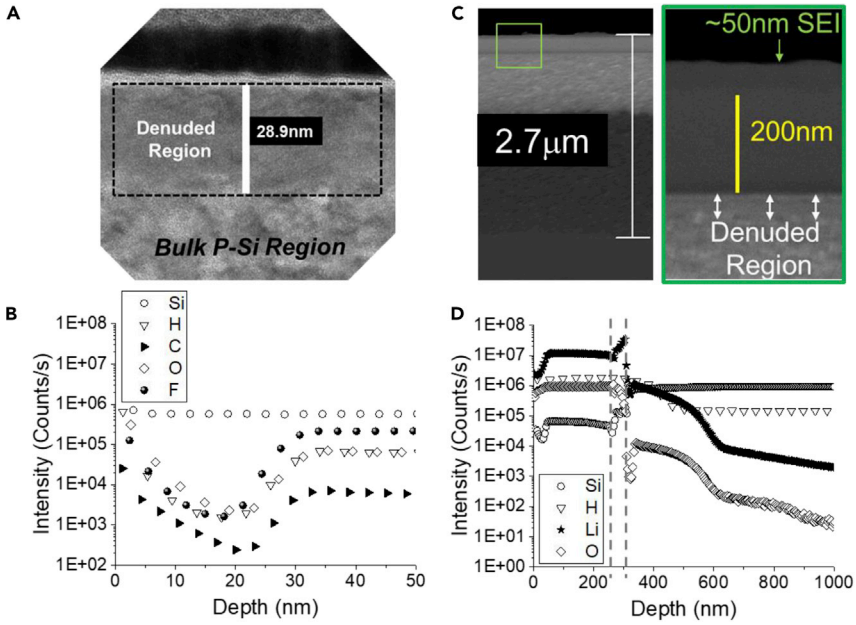

Figure 4. The Denuded Porous Crystalline Silicon Surface Layer and Utility as a Li-Barrier and Li-Metal Plating Layer

(A and B) (A) High-resolution transmission electron micrograph (TEM) of the denuded SC-PCS surface layer with accompanying (B) D-SIMS elemental results for initial 50 nm of substrate.

(C and D) (C) SEM cross section of an SC-PCS anode after 5 charge/discharge cycles and accompanying (D) D-SIMs elemental results for the initial 1000 nm of the cycled substrate—displaying a 2.7-μm SC-PCS + lithiated surface layers. Box indicates approximate area of higher-magnification SEM displaying the layered SEI/Li-metal/denuded layer/SC-PCS bulk interface. Dashed lines indicate approximate denuded layer region. Feature dimensions are illustrated with scale bars.

The top ~15 nm of the anodized silicon substrate is atomically quantified via XPS (Figure 5) for the same pre-cycled and 5 cycled SC-PCS anode, as well as for a 30 cycled SC-PCS anode to examine the robustness of the lithiated surface's SEI layer under extended cycling. As expected, and shown above with D-SIMS, the concentration of silicon significantly drops upon formation of Li-metal on the SC-PCS surface. The Si(2p) bonds are attributed to SiO_2 (103.0 eV) and Si-Si (99.3 eV), with a corresponding O(1s) SiO_2 bond at 532.5 eV (Shen et al., 2018) (Figure S6). Comparing lithium bond concentration between the 5^{th} and 30^{th} cycle a Li-surface layer decrease of 2.2 atomic % is observed, illustrating the near-constant Li-concentration in the stable SEI layer. Li—F bonds are also observed in the cycled electrode due to surface-adsorbed LiF as a standard inorganic SEI component (Yan et al., 2018). However, the lithium composition is dominated with lithium nitride species (Yan et al., 2018), due to N_2 exposure when utilizing an N_2 atmosphere glove box to deconstruct the post-cycled cells—thereby forming Li_3N at ambient temperature and obscuring the surface analysis of native lithium species (Thevenin and Muller, 1987). Oxygen comprises a significant atom % on the as-fabricated anode (Figure 5) due to the presence of silicon surface oxides (Figure S6). Upon cycling, a significant decrease in oxygen concentration is observed (31 atom % to 21 atom %), whereafter the oxygen concentration shows no significant change in concentration or composition for 30 cycles (Figure S6). $LiNO_3$ species (532.8 eV) and alkyl carbonate species (531.67 eV) $ROCO_2Li$ dominate the oxygen composition, again, due to N_2 exposure when utilizing an N_2 atmosphere glove box to deconstruct the post-cycled cells and *in situ* alkyl carbonate SEI formation, respectively. Fluorine decreases (~3 atom %) upon long-term cycling—where the primary loss is due to surface-adhered $LiPF_6$ with its accompanied electrolyte solvation shell (Figure S6: 688.1 eV, 686.4 eV)—leading to a slight increase in the stable presence of inorganic fluorine (e.g., LiF) species (Figure S6; ~688eV). Li, N, and P all display similar constant concentration trends upon cycling for 30 cycles, further indicating the stability of homogeneous lithium plating in the system (Lu et al., 2015a; Shen et al., 2020). As illustrated by Schnabel et al. (2020a, 2020b), the ability to maintain thin (<3-nm) layer of oxides on silicon, enables higher coulombic efficiency through the homogenization of lithiation processes—as evidenced by a thin resulting SEI layer containing low concentrations of P-F species. The suppression of surface oxide formation in conjunction with relatively high Si-H species

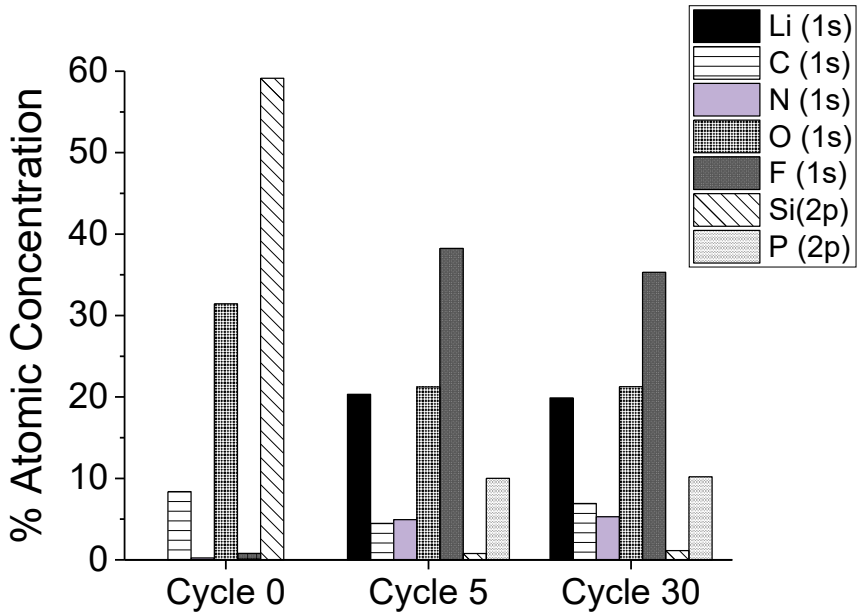

Figure 5. Percent Atomic Concentration as Calculated from XPS (See Figure S6 and Transparent Methods) for Pre-cycled and 5 and 30 Cycled SC-PCS Anodes

shown in the SC-PCS samples directly enables thin SEI layer formation with low (Figure S6; 30 cycles) and constant (Figure 5) concentration of P species upon cycling—contributing to a low-resistive, lithiophilic SC-PCS surface. Carbon is relatively abundant (~8 atom %) in the as-fabricated SC-PCS anodes—attributed to the carbon-containing solvents utilized in the post-anodization clean step (see Transparent Methods). There is a minor, 4.5 atom % to 6.9 atom %, increase in carbon content between the 5 cycled and 30 cycled anodes—attributed to minimal increase in SEI carbonate formation, in parallel with LiF, due to the reduction of the surface-adhered, organic electrolyte (Collins et al., 2015) which solvated the $LiPF_6$ species discussed above with the fluorine composition peaks. Carbon composition (not shown) consists of binding energies appearing at 284.7, 266.5, and 289.1 eV corresponding to aliphatic carbon, C-O, and C=O-related carbonate SEI bonds, respectively (Shen et al., 2018). Hence, SEI species indicate no surface instability or indication of Li-concentration anomalies (e.g., dendrite formation) on the Li-plated SC-PCS anode upon extended cycling—exemplifying the reversible efficacy of Li-plating/stripping on the SC-PCS anode.

Figure 6A displays a high-magnification SEM cross section showing the top lithium metal/denuded layer of the SC-PCS anode for the 30-cycled cell discussed in Figure 5. A thin, planarized Li-metal charge-barrier layer (16 nm) results from the SEM e-beam on the top surface of the ~37-nm denuded layer (Figure 6B). The beam of electrons in the scanning region concentrates electron density at the top surface of the highly conductive layer—while not resulting in Li-dendrite growth, thereby demonstrating the ability of the denuded layer to prevent surface dendrite growth and maintain an energetically favorable surface for planarized Li-metal plating even in the event of charge-concentration phenomena.

After 543 cycles (Figures 6C and 6D), only ~460 nm of the PCS bulk is displayed as lithiated, and a relatively thin Li-metal layer (267 nm) resides on the surface after the final discharge of the cell—confirming the long-term sustainability of the denuded layer to act as an effective Li-diffusion barrier. After hundreds of cycles, the denuded layer is able to protect the cell from destructive Li-Si volume expansion, while simultaneously enabling a stable Li-metal plating/stripping surface. The concentration of dead surface lithium (Figure 6D; 267 nm) at greater than 500 cycles is significantly low for a Li-metal electrode host (Jiao et al., 2018; Yan et al., 2016; Yang et al., 2015). Hence, even without pre-lithiation, the denuded top SC-PCS layer displays a novel mechanism where the denuded layer greatly suppresses the lithiation of the vacant high-surface-area SC-PCS, resulting in reversible Li-metal plating for at least 543 cycles.

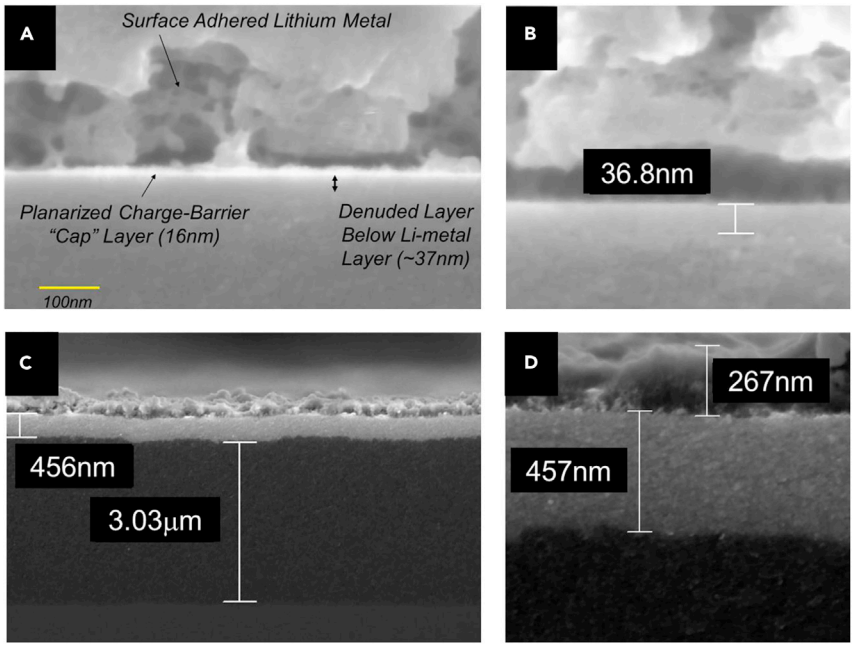

Figure 6. The Impact of the Denuded Region upon Progressive Lithiation of Non-pre-lithiated SC-PCS

(A) SEM cross section showing interface of denuded/bulk porous silicon regions from 200 s anodized SC-PCS anode after 30 charge/discharge cycles.

(B) High-magnification SEM of (A) displaying well-formed ~37-nm denuded region.

(C) SEM cross section of 543 charge/discharge cycled SC-PCS anode.

(D) High-magnification SEM of sample from (C) displaying 267 nm of "dead" lithium metal residing on a 457-nm lithiated portion of the bulk porous silicon. Feature dimensions are illustrated with scale bars.

Comparatively, when directing the electron-dense SEM beam on the top of the plated Li-metal surface, not at the denuded surface layer, as in Figures 6A and 6B, Li-dendrites are easily formed via exposure to the focused SEM electron beam (Figure 7A). Exceptional, flexible barrier protection of the SC-PCS-bulk is displayed from the denuded layer—where induced Li-dendrite formation only grows into the open space above the Li-metal layer and not into the SC-PCS bulk. As indicated in Figure 7A, the denuded layer flexibly bends in response to the stress induced from the e-beam electron density—thereby preventing Li-metal growth deeper into the substrate and protecting both the bulk PCS below.

Figure 7B illustrates a ~280-nm Li-metal layer, which was grown in and on the denuded layer after the cell was stopped before completing the first hour of pre-lithiation with Li-metal foil (see Transparent Methods)—illustrating the ability of the porous denuded layer to space-fill with lithium metal and maintain a stable planarized Li-metal layer above, while simultaneously preventing the majority of Li-ions from accessing the SC-PCS bulk.

Fully pre-lithiated SC-PCS anodes show homogeneous Li-metal plating on the denuded layer (1.13 µm) and within the PCS bulk, such as the full cell cycled 6 times as shown in the discharge state in Figure 7C. Even the non-pre-lithiated SC-PCS anode that displays SC-PCS degradation below the denuded layer maintains a planarized layer "dead" Li-metal after 330 cycles (Figure 7D). The minimal (0.40 µm) growth of "dead" Li-metal, along with the excellent planarity observed after 330 cycles, validates the sustainability of the denuded layer in both preventing dendrite formation and suppressing the formation of irreversible dead lithium, even while the PCS bulk is undergoing degradation.

Figure 8 displays the half-cell performance of both Li-metal/SC-PCS (Figure 8A) and Li-metal/LCO (Figure 8B) formulations during the initial 45 cycles. High capacity can be maintained with the LCO half-cell (Figure 8B), yet only at low C-rates. In contrast, the SC-PCS anode (Figure 8A) displays a minimal decrease in capacity at twice the rate—illustrating the robust electrochemical integrity of the SC-PCS anode over the LCO cathode. In addition, Figure 8C displays the coulombic efficiency for both half-cell formulations.

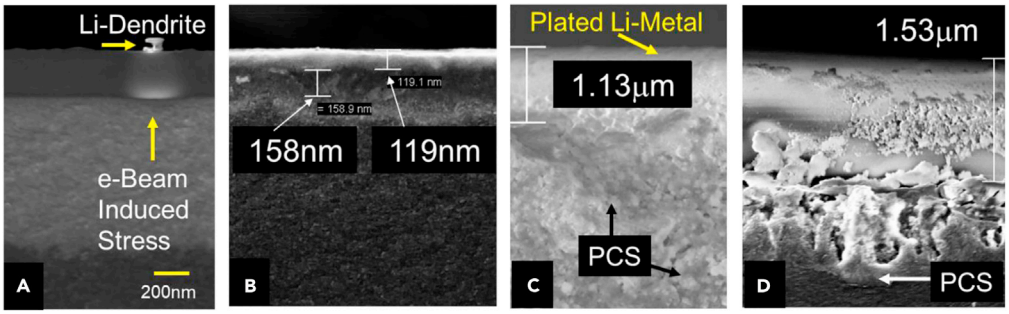

Figure 7. The Electrochemical Plating and Barrier Properties of the Electrochemically Cycled Denuded SC-PCS Layer

(A) The ability to induce dendrites with an SEM electron beam in an SC-PCS anode that has been lithiated after 5 charge discharge cycles. Li-dendrite formation only occurs in the upward direction, where the denuded region at the bulk PCS interface elastically flexes to the increased electron density, preventing lithium from diffusing into bulk PCS.

(B) Partially pre-lithiated SC-PCS anode displaying the growth of planarized Li-metal on the SC-PCS denuded layer.

(C) Plated Li-metal layer on pre-lithiated SC-PCS anode after the 6th discharge cycle.

(D) Plated Li-metal layer on non-pre-lithiated SC-PCS anode after the 330th discharge cycle. Features are indicated and dimensions illustrated by scale bars.

Overall, the SC-PCS half-cell has a higher average coulombic efficiency (97.4%) compared with the LCO half-cell—indicating the superior electrochemical integrity and reversible capacity of the SC-PCS anode compared with the inefficiency of the common cathode. However, the first cycle of the SC-PCS half-cell displays low coulombic efficiency (~30%) due to a lengthy formation process—thereby indicating a significant need for pre-lithiation to effectively advance cell efficiency. Hence, with the implementation of a pre-lithiated controlled formation process, the pre-lithiated SC-PCS anode is expected to perform very well at high discharge rates with a cathode-efficiency-limited cycle life.

Performance of Pre-lithiated Denuded Porous Silicon Full Cells

Electrochemical pre-lithiation was employed to lithiate through the denuded region and into the PCS bulk, in a slow, controlled fashion (see Transparent Methods). Figure 9 illustrates the five stages of the electrochemical pre-lithiation of SC-PCS. Stage 1 (Figure 9A) is the initial lithiation of the NPH_x-containing denuded layer, requiring over a volt of overpotential to initially lithiate the PCS anode. Stage 2 (Figure 9B) displays a voltage energy barrier that is overcome beginning at roughly 1.8 V, when the nanoporous denuded region fills with lithium species—as indicated by the slight increase in voltage back to 2.0 V. Stage 3 shows the energy barrier associated with the initial filling of lithium in the SC-PCS bulk, below the denuded layer, as indicated by the slight voltage increase (hump) starting at ~1.25 V and maximizing at ~1.40 V. As the process continues, the bulk SC-PCS continues to be lithiated deeper into the substrate. At approximately 0.6 h, a voltage minimum is achieved (0.045 V) followed by a final voltage energy barrier, stage 4 (Figure 9C), indicating the arrival of the lithium species at the porous crystalline/non-porous crystalline wafer interface. The remaining ~8h of the pre-lithiation process fills the bulk SC-PCS above the porous crystalline/non-porous crystalline interface.

The electrochemical pre-lithiation shows homogeneous and well-integrated lithiation throughout the entire PS anode (Figure 10A), including the top surface-denuded region (Figure 10B), and at the PCS/crystalline silicon bulk interface (Figure 10C). The bulk lithiated PS retains its robust porous nature upon full lithiation—with visible lithium species observed throughout the PCS bulk (Figure 10D). Thus, the denuded PS samples easily achieve homogeneous distribution of lithium during the standard low-rate pre-lithiation process (see Transparent Methods). The controlled lithiation of the substrate is enabled by the diffusion-barrier properties of the denuded region—resulting in the controlled five stages of the pre-lithiation discussed above and enabling uniform lithiation of the bulk PCS. The single formation process minimizes cell inefficiencies from irreversible Li-capacity experienced from repeated surface reaction (formation) processes experienced on subsequent cycling—as Figures 6C and 6D demonstrate above. Pre-lithiation of SC-PCS enables a far more efficient and higher performing cell, as the Li_xSi formation process within PS is limited to a single event without the consumption of irreversible lithium from the cathode upon subsequent cycling. The pre-lithiated SC-PCS can now effectively facilitate extended Li-metal plating at a

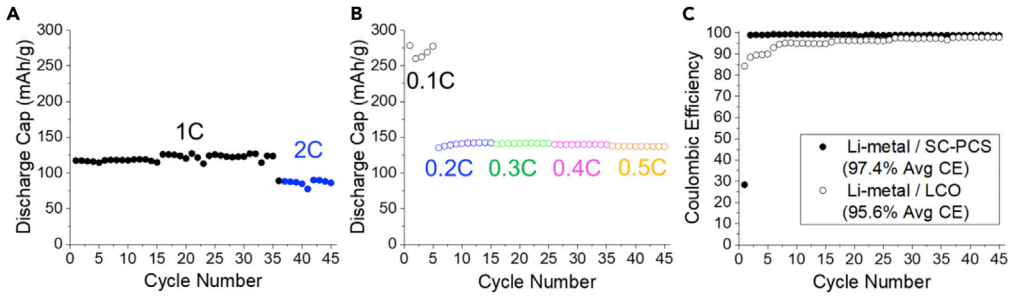

Figure 8. The Efficiency of Full Cell Components as Explored with Half-Cell Configurations
(A and B) (A) Li-metal/SC-PCS and (B) Li-metal/LCO half cells for initial 45 cycles at indicated C-rates.
(C) Coulombic efficiency of both (A) and (B).

higher efficiency and longer cycle life due to the passivation (Li_xSi formation) of reactive silicon within the SC-PCS bulk.

Voltage profiles for an electrochemically pre-lithiated SC-PCS anode in full cell configuration with an NMC 811 cathode are shown in Figure 11. All charge/discharge profiles are generated at a C-rate of 0.3. Figure 11A shows the initial cycle after pre-lithiation, displaying an initial charge overpotential (3.8V) with an extended charge saturation plateau—indicating further space filling of the pre-lithiated Li_xSi SC-PCS bulk. By the second charge cycle (Figure 11B), the charge overpotential is significantly reduced (3.4V), along with charge saturation—revealing a less-resistant SC-PCS anode where denuded surface plating (~4.0V–4.2V), Li_xSi plating (Chen et al., 2019) (~3.75V–4.0V), and Li_xSi intercalation (3.4V–3.75V) increase in concentration leading to proportional discharge capacity and energy density increases. The 20th charge cycle (Figure 11C) displays an even smaller charge overpotential (~3.3V), augmented Li_xSi intercalation (3.4V–3.65V) and Li_xSi plating (~3.65–3.95V) stages, extended denuded surface layer (3.95V–4.2V) plating stage, and a very short charge saturation step—illustrating the establishment of stable bimodal charge plating mechanisms after 20 cycles and yielding the highest capacity and energy density (680 Wh/kg) shown. Upon discharge, the internal resistance of the cell is shown to decrease, as shown by a 0.10 V increase in discharge onset potential (4.05V–4.15V), during the initial 20 cycles. Complimentary voltage ranges of Li-metal denuded layer stripping (~4.15V–~3.85V), Li_xSi stripping (~3.85–~3.35V), and Li_xSi deintercalation (3.35–2.7V) discharge processes are shown to change proportionally with charge cycling increases until the 20th cycle—further indicating the stability of the hybrid plating/stripping and intercalation/deintercalation SC-PCS charge storage processes.

Cycles 50 to 250 of this cell utilized an increased C-rate of 0.5C, displaying capacity fade due to higher C-rate-induced degradation of electrode structure. Cycles 250 to 900 utilized the original 0.3C rate, which mitigated degradation, yet maintained lower capacity due to the prior irreversible structure breakdown and associated capacity loss. By the 300th cycle (Figure 11D) the charge saturation step has increased again, resulting in a permanent ~14% decrease in discharge capacity induced by higher C-rates. Cycle 300 displays a voltage and capacity fade mechanism similar to Chen et al. (2019) where diminished Li-metal charge storage results from the increasing presence of Li_xSi delithiation processes, and inherent to the current work, accompanied by a relative decrease in concentration of denuded layer stripping, when the cell is cycled at higher C-rates. Hence, the suppression of Li_xSi delithiation processes in pre-lithiated SC-PCS anodes enables sustainably high average energy density (587 Wh/kg), discharge voltage (3.43 V), and discharge capacity (169 mAh/g) for 300 cycles at low to mid C-rates.

A variety of SC-PCS full cell formulations (Figure 12) were compared to investigate performance impact with respect to anodization time (A: 200 s, B: 500 s, C: 500 s, D: 4,800 s), cathode capacity (A–C: LCO, D: NMC), pre-lithiation (C & D), and backside anode electrochemical protection through the use of a Li-blocking (Collins et al., 2020b) metal encapsulation layer (D). The parasitic impact of non-pre-lithiation is shown with the 200 s PS anode (Figure 12A) having significantly higher average capacity and coulombic efficiency (Figure S7) than the 500 s PS cell with far greater SC-PCS Li-vacancy (Figure 12B). Without pre-lithiation, the cell continues to progressively mobilize the formation process deeper

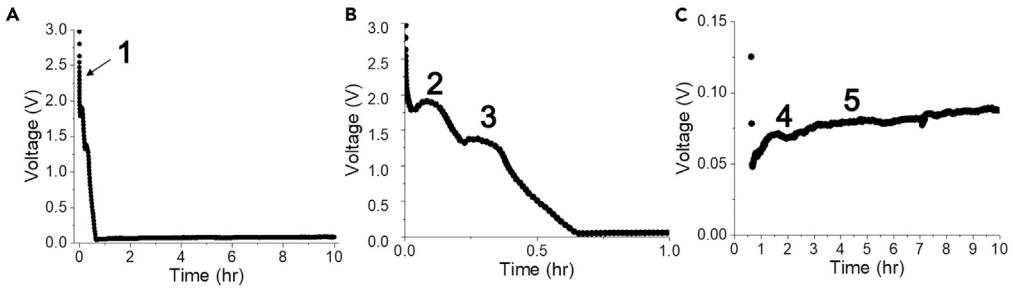

Figure 9. Five-Stage Electrochemical Pre-lithiation of SC-PCS

Stages are displayed with voltage versus time in (A) full 10 h time range, (B) early time stage, and (C) low-voltage range. (1) Initial lithiation of the SC-PCS anode, (2) initial lithiation of the NPHx containing denuded SC-PCS, (3) initial lithiation of the PCS bulk below the denuded porous layer, (4) lithiation at the SC-PCS/crystalline silicon-wafer interface, (5) lithiation in the SC-PCS bulk and on the denuded surface layer.

through the substrate—thereby incrementally accessing newly electrochemically accessed PCS bulk and continuously creating irreversible and morphologically damaging Li_xSi species with every progressive cycle. However, the 500 s PS anode lasts roughly twice as long as the 200 s anode, because the substrate has >2× the PCS thickness to protect lithium from interaction with the underlying crystalline silicon wafer.

Electrochemical pre-lithiation was administered to both 500 s (Figure 12C) and 80 min (Figure 12D) PS anodes before their full cell assembly with thick LCO (160 μm) and NMC (100 μm) cathodes, respectively (see Transparent Methods). High C-rate (1C) discharge capacity at significantly higher coulombic efficiency (94.1%) and >100 mAh/g average capacity was achieved when the pre-lithiated analog of the Figure 12B cell was employed (Figure 12C). The significant performance increase is attributed to the "single and slow" formation process, which occurs during pre-lithiation, resulting in far lower Li_xSi formation and associated irreversible capacity.

When using a high-capacity NMC cathode, with a ~34 μm pre-lithiated SC-PCS anode (Figure 12D), competitively high average capacity (165 mAh/g) and coulombic efficiency (97.1%) is achieved at mid to high C-rates for 350 cycles. Any potential parasitic reactions experienced at the backside of the Si-substrate are suppressed, via the use of Li-corrosion-suppressing, Li-blocking (Collins et al., 2020b) metal (Figure S8). At mid C-rates (0.3C), the coulombic efficiency climbs to 99.9% within 5 cycles, and remains at 99.9% for the initial 50 cycles, as indicated in Figure 12D. However, the subsequent 200 cycles employ a higher C-rate (0.5C) where a higher rate of Li_xSi reaction leads to capacity fade and decreased coulombic efficiency (Figure S7D). Hence, the homogeneous pre-lithiation of 80-min anodized thick SC-PCS, coupled with backside

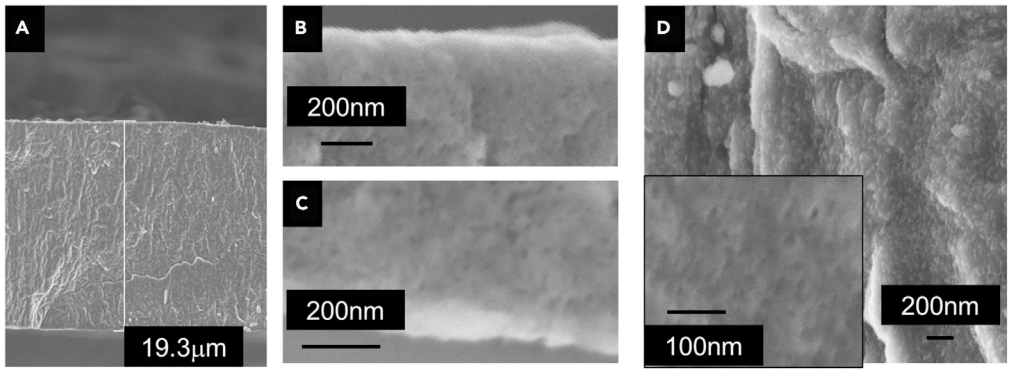

Figure 10. Electrochemical Pre-lithiation of Standard Cleaned Porous Crystalline Silicon (SC-PCS)

(A) SEM cross section of electrochemically pre-lithiated SC-PCS (~40 min anodization; 19.3 μm).
(B and C) (B) Top surface and (C) bottom porous/crystalline bulk interface of electrochemically pre-lithiated SC-PCS.
(D) SC-PCS bulk with high magnification of lithiated pores (inset). Feature dimensions are illustrated with scale bars.

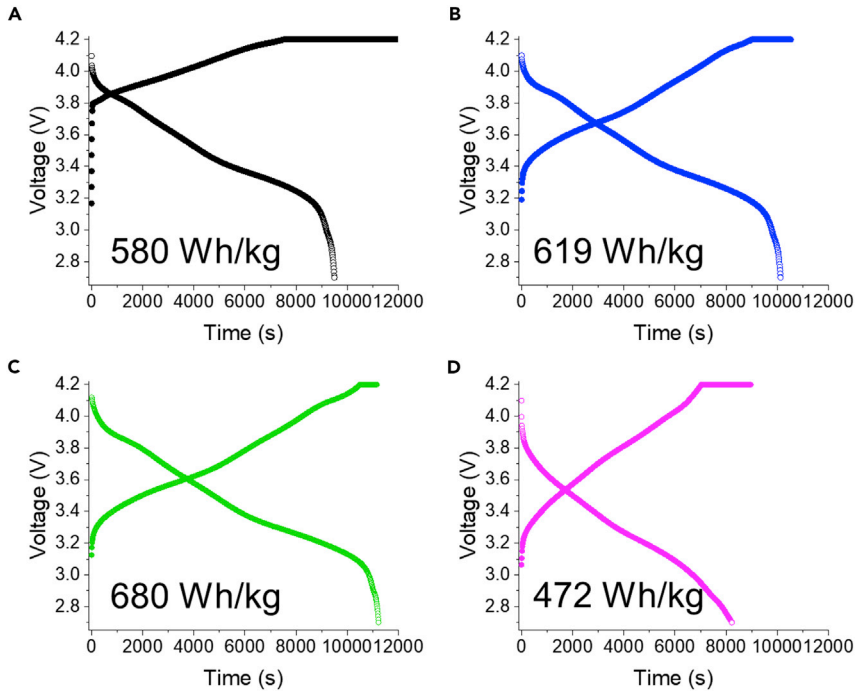

Figure 11. Charge and Discharge Voltage Profiles for Pre-lithiated 100 μm NMC811/80 min SC-PCS Full Cell
Voltage profiles for cycles (A) 1, (B) 2, (C) 20, and (D) 300 are displayed. Energy density (based on NMC811 active cathode mass) is indicated for each discharge profile.

wafer Li-protection, enables a full cell with Li-metal competitive energy density and capacity, whereas combining mid and high C-rates upon extended cycling yields 900 cycles with an average capacity of 125mAh/g (Figure S9).

Post cycled SEM cross sections of the four cells are displayed in Figure 13. The 200 s anodized SC-PCS (Figure 13A) experiences an extremely significant amount of irreversible Li_xSi formation, resulting in excessive mechanical volume expansion and separation where the active anode expands to roughly 215× its original ~3 μm thickness. The mechanical expansion of the anode results in permanent adhesion to the cell separator (indicated with black arrow). The 500 s anodized SC-PCS cell (Figure 13B), stopped after twice as many cycles as Figure 13A, displays a relatively meager ~7× PS volume expansion relative to fabricated thickness (~6μm)—illustrating the positive impact of thicker SC-PCS upon long-term cycling in preventing the Li_xSi volume changes and associated mechanical breakdown (e.g., observed via cracks in SC-PCS).

The same post cycled PS thickness is observed for the same cell formulation (500 s anodization); however, significant differences are observed with the pre-lithiation analog (Figure 13C). The SEM of the pre-lithiated version (Figure 13C) displays no high-resistance mechanical separation or cracking after 2,230 cycles. The controlled, homogeneous formation process delivered by pre-lithiation forms a robust pore structure with high electrochemical activity, which does not break down under intense rates (1C: 1 h to fully discharge) and long-term cycling. In addition, the robust, pre-passivated Li_xSi pore structure created by the single formation event enables a highly flexible, expansion-stress-compensating pore structure (Figure 13C; 4.42-μm pore), thereby explaining the lack of mechanical separation observed in this cycled anode. Hence, the same ~7× volumetric thickness increase is observed in the pre-lithiated (Figure 13C) SC-PCS as was observed in the non-pre-lithiated SC-PCS anode (Figure 13B), yet at roughly 10× the C-rate (Figure 12) and more than 6× the cycle life (2,330 cycles) without any SC-PCS degradation or cracking.

When utilizing a Li-blocking metal for protecting surface reactions on the wafer backside, coupled with the use of very thick PS (~34 μm) and a high-loading-capacity cathode (NMC811)—merely a ~2.3× expansion in PS volume results after 900 cycles (Figure 13D). The SC-PCS and crystalline wafer bulk regions are fully

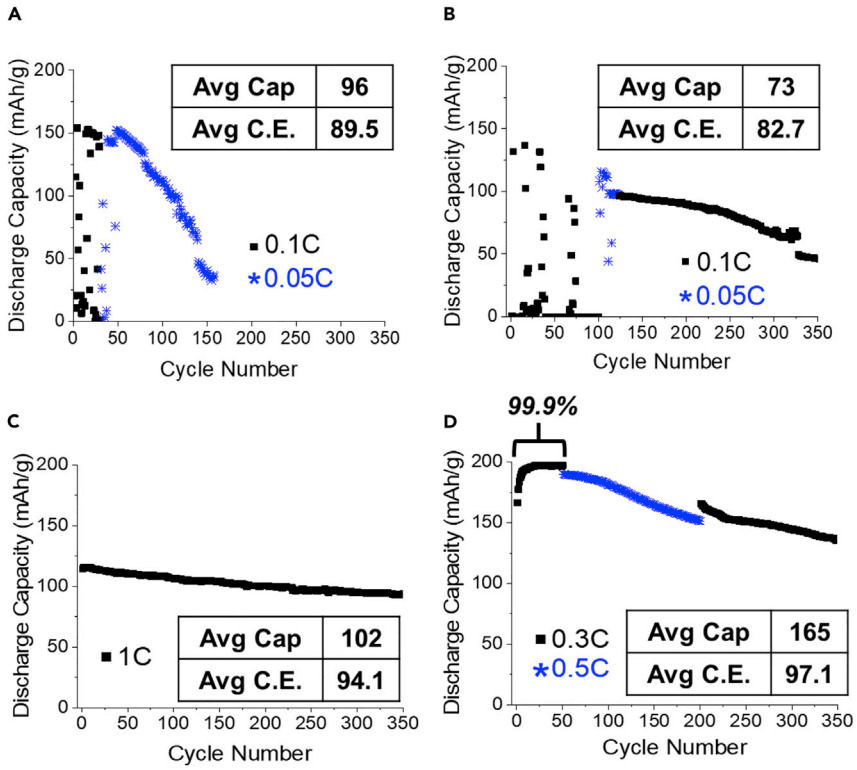

Figure 12. Extended Discharge Capacity of SC-PCS Full Cells, Related to Figure S7 (Coulombic Efficiency)

(A–D) Non-pre-lithiated full cells containing 160 μm LCO cathode and SC-PCS (A) 200 s and (B) 500 s anodized SC-PCS anodes. Electrochemical pre-lithiated SC-PCS full cells with (C) 160 μm LCO cathode/500 s anodized SC-PCS anode and (D) 100 μm NMC811 cathode/80 min anodized SC-PCS anode containing a backside deposited Li-blocking metal layer. Average specific capacity (mAh/g) and % coulombic efficiency are displayed.

intact upon long-term cycling in a complete, unitary fashion. No particle separation is observed in the expanded SC-PCS (80.9 μm) with virtually no observable pore expansion due to the compensation from the relatively thick and highly Li_xSi surface-passivated ~34-μm-thick original SC-PCS layer. However, the formation of new Li_xSi sites due to the higher C-rate applied during cycles 51 to 250 concentrates irreversible capacity in the bulk until 900 cycles, transforming the SC-PCS anode into a stable Li_xSi formation reservoir, yet progressively decreases cell efficiency and capacity. Hence, the relative SC-PCS thickness, in pre-lithiated cells is proportional to the cell's ability to "stress relieve" or greatly delay increases in resistivity due to irreversible lithium or any reversible Li_xSi reactions—thereby significantly extending cycle life. Notably, the pre-lithiated SC-PCS shows no dead lithium or dendrite formation on the SC-PCS surface (Figure 13D) after 900 cycles, even with the observed capacity fade (Figure S9).

Electrochemical Impedance Spectroscopy of Tested Full Cells

Control of mechanical failure and separation is of utmost importance when fabricating silicon anode full cells. As illustrated above, the use of pre-lithiation and thick SC-PCS integrated into crystalline silicon wafers enables competitively high performance for 350 cycles (Figure 12D). However, the total cycle life of the cell is nearly 1,000 cycles (Figure S9). To better understand the resistance impact of the silicon anode on the full cell's performance, electrochemical impedance spectroscopy (EIS) was conducted on the best (Figure 12D) and worst (Figure 12A) cycled cells described above (Figure 14). EIS was conducted at three different stages in each cell's life (early, mid, and late cycling stages). Nyquist plots displayed two distinct time constant regions for each cell formulation (Figures 14A and 14B), with two associated resistance values (R_1 and R_2) calculated through simple half circle fits. Average resistivity was calculated over all three stages for both cell's R_1, R_2, and full cell resistivity values (Figure 14C). Even after 900 cycles, the total resistance to transfer charge through the cell is 41% lower for the pre-lithiated, thick SC-PCS cell, compared with the non-pre-lithiated, thin SC-PCS cell, which lasted only 156 cycles. The primary contributor to cell resistance

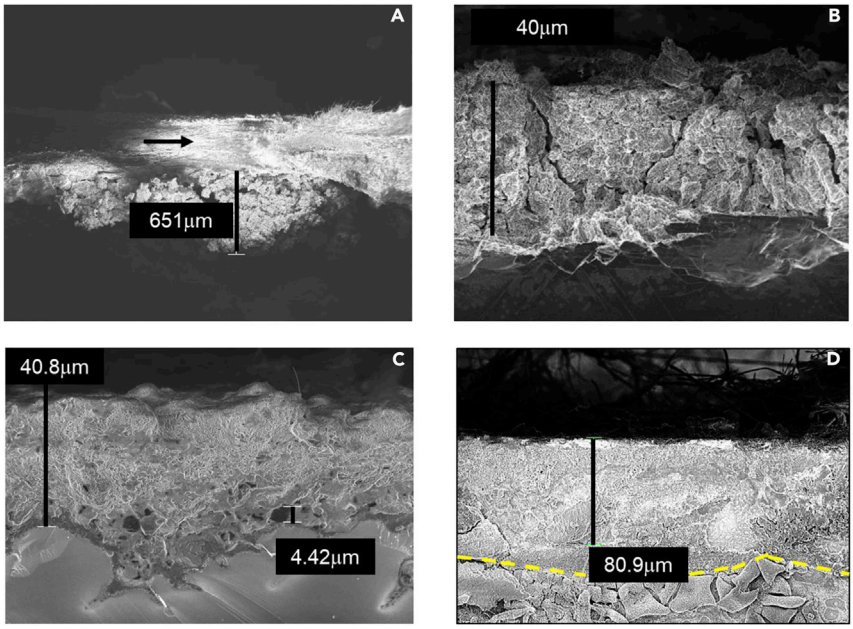

Figure 13. Post-cycled SEM Cross Sections of Four SC-PCS Anode Formulations after Extended Cycling

(A–D) Non-pre-lithiated 160 μm LCO cathode containing full cells originally containing (A) 200 s and (B) 500 s anodized SC-PCS anodes. Arrow indicates separator attached to porous silicon anode. Electrochemical pre-lithiated SC-PCS full cells with originally (C) 160 μm LCO cathode/500 s anodized SC-PCS anode and (D) 100 μm NMC811 cathode/80 min anodized SC-PCS anode with Li-blocking metal-protected anode backside. Dotted line displays interface between porous silicon and the bulk silicon substrate. Feature dimensions are illustrated with scale bars.

(R_2) is associated with cell components other than the SC-PCS anode surveyed at mid to lower frequencies (e.g., cathode, etc.). The pre-lithiated, thick SC-PCS (final thickness: 80.9 μm) cell displays an average R_2, which is 45% less in resistance compared with the non-pre-lithiated, relatively thin SC-PCS (final thickness: 651 μm). The non-pre-lithiated cell exhibits poor diffusivity as observed with low-frequency region curving into the real resistance x-axis—indicating the deleterious impact of cell component compression, due to the significant SC-PCS volume expansion in non-pre-lithiated full cells. The average SC-PCS anode resistivity (R_1) is 27% lower for the 900 cycled pre-lithiated cell (original SC-PCS thickness: ~34 μm), compared with the 156 cycled non-pre-lithiated cell (original SC-PCS thickness: ~2.4 μm)—further solidifying the long-term sustainability in combining controlled pre-lithiation formation with thick SC-PCS anodes. Hence, effective integration of thick PS anodes combined with the controlled Li-metal and Li_xSi formation, presented herein, enables SC-PCS anodes to sustainably plate Li-metal in and on SC-PCS anodes without negative impact of Si-volume increases or dendrite hazard resulting in a low-resistivity cell with electrochemical performance on the order of Li-metal batteries.

Conclusion

PCS anodes were anodized into wafer-level p+ silicon in a completely unitary fashion. Pre/post anodized surface cleaned substrates, with subsequent electrochemical pre-lithiation, were shown to significantly improve the crystallinity and electrochemical performance of the SC-PCS anodes through the removal of oxygen heteromaterial and $O_xSi—H_y$ defect species. In addition, a high concentration of nano-pore (NPH_x) Si-H_x species remained, which enabled lithiophilic *in situ* electrochemical properties, with the topmost nanopore layer acting as a planar, dendrite-suppressing surface for Li-metal plating and as a Li-ion diffusion barrier, which minimized the expansion/contraction-related stress experienced on the SC-PCS anode throughout the lifetime of full cells. A highly sustainable porous crystalline anode resulted where lithium was reversibly plated on the porous denuded layer as well as within the SC-PCS bulk due to passivated Li_xSi surface species formed during pre-lithiation.

In addition to safety and performance attributes competitive with state-of-the-art Li-metal anode batteries, the SC-PCS fabrication method has three main advantages over other silicon anode designs. First, we

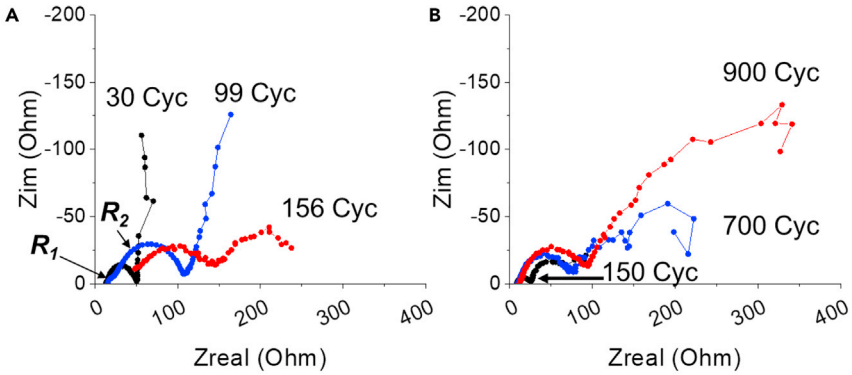

C

Anode	SC-PS Original Thickness (μm)	Cycle Life	R_1 Avg (Ω*cm²)	R_2 Avg (Ω*cm²)	Cell Transfer Ω (R_{1Avg}+R_{2Avg}) (Ω*cm²)
200s Anodization Non-Pre-Lithiated	~2.5	156	33	153	185
4800s Anodization Pre-Lithiated	~34	900	24	84	108

Figure 14. Resistivity Impact of Thin Non-pre-lithiated SC-PCS and Thick, Pre-lithiated SC-PCS Anode Containing Full Cells

Electrochemical impedance spectroscopy (EIS) of (A) 160 μm LCO cathode/thin (200 s anodized) non-pre-lithiated SC-PCS anode containing full cell and (B) 100 μm NMC811 cathode/thick (4800 s anodized) pre-lithiated SC-PCS anode containing full cell over the course of their cycle life. The cycle number at which each Nyquist plot was acquired is indicated, along with the semicircular regions utilized to calculate the R1 (high-frequency region; SC-PCS anode) and R2 (mid-low-frequency region; non-anode mass transfer cell components) resistivities.

(C) Table displaying the approximate original SC-PCS thickness, cycle life, average R1 and R2, and cumulative charge transfer resistivity for both cells.

achieve silicon wafer-scale integration of SC-PCS containing an embedded lithiophilic surface layer using standard semiconductor processes—necessitating no further composite formulation or processing and resulting in a pure silicon anode. Second, when combined with pre-lithiation, the lithiophilic surface layer effectively suppresses dendrite formation while simultaneously minimizing Li-diffusion into the SC-PCS bulk, preventing cell failure via volume expansion or mechanical breakdown, and resulting in a safe and sustainable wafer-integrated silicon anode. Third, the bimodal Li-plating mechanism (surface and bulk) enables energy density (587 Wh/kg; 300 cycles), capacity (169 mAh/g; 300 cycles), and resistivity for 900 cycles (24 Ω*cm^2), which is competitive with Li-metal anode batteries. Our proof-of-concept batteries yield comparable performance with recent reports of Li-plating on silicon host-anode full cells, but notably using only silicon as active material, without the use of additives, slurries, binders, powders, or composite processing. The dual porous layered wafer-integrated SC-PCS anode displays competitive leading full cell performance (195 mAh/g; 99.9% coulombic efficiency) for the initial 50 cycles when compared with commercial NMC811 | graphite anode analogs—serving as a prototype to long-lasting, wafer-scalable silicon host batteries with performance metrics at Li-metal caliber, yet without the presence of hazardous, uncontrollable Li-metal foil anodes.

Limitations of the Study

Further work in testing and development is needed to advance both a C-rate higher than C/3 before onset of capacity fade and specifics regarding the mechanisms of Li_xSi species formation/degradation and Li-plating within the SC-PCS bulk to advance cell coulombic efficiency at all C-rates.

Resource Availability

Data and Code Availability

The data that supports the findings of this study are available from the corresponding authors upon reasonable request.

Lead Contact
John Collins 3dsurfacechem@gmail.com.

Materials Availability
The materials that support the findings of this study are available from the corresponding authors upon reasonable request.

METHODS
All methods can be found in the accompanying Transparent Methods supplemental file.

SUPPLEMENTAL INFORMATION
Supplemental Information can be found online at https://doi.org/10.1016/j.isci.2020.101586.

ACKNOWLEDGMENTS
IBM Research would like to thank Ganesh Skandan, Paramesh Chinnam, and Anantharam Navulla as well as all other helpful personnel from NEI Corporation for their assistance in material supplies and fabrication.

AUTHOR CONTRIBUTIONS
D.K.S., J.P.d.S., and J.C. conceived idea and designed the experiments. D.K.S. directed the project. J.C., J.P.d.S., M.H., J.A.O., and S.W.B. carried out the experiments and data acquisition. J.C. wrote the paper with input from coauthors. J.C., J.P.S., M.H., J.A.O., and S.W.B. carried out the data analysis. J.C. and D.K.S. are the corresponding authors.

DECLARATION OF INTERESTS
International Business Machines (IBM) has several patents pending relating to this work.

Received: July 29, 2020
Revised: September 1, 2020
Accepted: September 16, 2020
Published: October 23, 2020

REFERENCES
An, W., Gao, B., Mei, S., Xiang, B., Fu, J., Wang, L., Zhang, Q., Chu, P.K., and Huo, K. (2019). Scalable synthesis of ant-nest-like bulk porous silicon for high-performance lithium-ion battery anodes. Nat. Commun. *10*, 1447.

Athanasiou, C.E., Jin, M.Y., Ramirez, C., Padture, N.P., and Sheldon, B.W. (2020a). High-toughness inorganic solid electrolytes via the use of reduced graphene oxide. Matter *3*, 212–229.

Athanasiou, C.E., Zhang, H., Ramirez, C., Xi, J., Baba, T., Wang, X., Zhang, W., Padture, N.P., Szlufarska, I., and Sheldon, B.W. (2020b). High toughness carbon-nanotube-reinforced ceramics via ion-beam engineering of interfaces. Carbon *163*, 169–177.

Buttard, D., Bellet, D., and Dolino, G. (1996). X-ray-diffraction investigation of the anodic oxidation of porous silicon. J. Appl. Phys. *79*, 8060–8070.

Buttard, D., Dolino, G., Faivre, C., Halimaoui, A., Comin, F., Formoso, V., and Ortega, L. (1999). Porous silicon strain during in situ ultrahigh vacuum thermal annealing. J. Appl. Phys. *85*, 7105–7111.

Chae, S., Choi, S.-H., Kim, N., Sung, J., and Cho, J. (2020). Integration of graphite and silicon anodes for the commercialization of high-energy lithium-ion batteries. Angew. Chem. Int. Ed. *59*, 110–135.

Chen, J., Fan, X., Li, Q., Yang, H., Khoshi, M.R., Xu, Y., Hwang, S., Chen, L., Ji, X., Yang, C., et al. (2020). Electrolyte design for LiF-rich solid–electrolyte interfaces to enable high-performance microsized alloy anodes for batteries. Nat. Energy *5*, 386–397.

Chen, L., Fan, X., Ji, X., Chen, J., Hou, S., and Wang, C. (2019). High-energy Li metal battery with lithiated host. Joule *3*, 732–744.

Collins, J. (2014). Tuning Carbon Microstructure for Advancing Electrochemical Energy Storage (Dissertation) (University of Massachusetts Boston).

Collins, J., Afzali-Ardakani, A., Papalia, J., Souza, J.D., Todorov, T., Pacquette, A., Krishnan, M., Rozen, J., Sadana, D.K., 2019. Silicon encapsulated all solid-state Li-ion microbatteries. Meet. Abstr. MA2019-01, 58.

Collins, J., Afzali-Ardakani, A., Papalia, J.M., Sadana, D.K., 2020a. Lithium Energy Storage Devices. US20200212492A1.

Collins, J., de Souza, J.P., Lee, Y.S., Pacquette, A., Papalia, J.M., Bishop, D.M., Todorov, T., Krishnan, M., Joseph, E., Rozen, J., and Sadana, D. (2020b). Fundamentals, impedance, and performance of solid-state Li-metal microbatteries. J. Vacuum Sci. Technol. A *38*, 033212.

Collins, J., Gourdin, G., Foster, M., Qu, D., 2015. Carbon surface functionalities and SEI formation during Li intercalation. Carbon, Carbon Materials in Energy Storage and Conversion, Dedicated to the 5th Anniversary of the School of Energy at Soochow University 92, 193–244.

Collins, J., Gourdin, G., and Qu, D. (2018). Chapter 3.23 - modern applications of green chemistry: renewable energy. In Green Chemistry, B. Török and T. Dransfield, eds. (Elsevier), pp. 771–860.

Collins, J., Krishnan, M., Bedell, S., PACQUETTE, A.L., Papalia, J., TODOROV, T., 2020c. Fabrication of All-Solid-State Energy Storage Devices. US20200212491A1.

Collins, J., Krishnan, M., Papalia, J., Bruce, R., PACQUETTE, A.L., 2020d. Through Silicon via Energy Storage Devices. US20200212383A1.

Collins, J., Ngo, T., Qu, D., and Foster, M. (2013). Spectroscopic investigations of sequential nitric acid treatments on granulated activated carbon: effects of surface oxygen groups on π density. Carbon *57*, 174–183.

Collins, J., Souza, J.P.de, Sadana, D.K., 2020e. Silicon Substrate Containing Integrated Porous Silicon Electrodes for Energy Storage Devices. US20200020895A1.

Collins, J., Zheng, D., Ngo, T., Qu, D., and Foster, M. (2014). Partial graphitization of activated carbon by surface acidification. Carbon *79*, 500–517.

Cui, C., Yang, C., Eidson, N., Chen, J., Han, F., Chen, L., Luo, C., Wang, P.-F., Fan, X., and Wang, C. (2020). A highly reversible, dendrite-free lithium metal anode enabled by a lithium-fluoride-enriched interphase. Adv. Mater. *32*, 1906427.

Fahlman Bradley, D., and Ramírez-Porras, A. (2012). Surface-functionalized porous silicon wafers: synthesis and applications. Adv. Chem. Sens. *Chapter 7*, 153–168.

Fan, X., Chen, L., Borodin, O., Ji, X., Chen, J., Hou, S., Deng, T., Zheng, J., Yang, C., Liou, S.-C., et al. (2018). Non-flammable electrolyte enables Li-metal batteries with aggressive cathode chemistries. Nat. Nanotechnol. *13*, 715–722.

Ferrari, A.C., and Robertson, J. (2000). Interpretation of Raman spectra of disordered and amorphous carbon. Phys. Rev. B *61*, 14095–14107.

Fu, J., Yu, P., Zhang, N., Ren, G., Zheng, S., Huang, W., Long, X., Li, H., and Liu, X. (2019). In situ formation of a bifunctional interlayer enabled by a conversion reaction to initiatively prevent lithium dendrites in a garnet solid electrolyte. Energy Environ. Sci. *12*, 1404–1412.

Gardner, D.S., Holzwarth, C.W., Liu, Y., Clendenning, S.B., Jin, W., Moon, B.-K., Pint, C., Chen, Z., Hannah, E.C., Chen, C., et al. (2016). Integrated on-chip energy storage using passivated nanoporous-silicon electrochemical capacitors. Nano Energy *25*, 68–79.

Ghannam, M.Y., Hassan, M.M., DePauw, V., Beaucarne, G., Poortmans, J., and Mertens, R. (2008). Study and estimation of the residual stress in porous silicon layer formed on the surface of a crystalline silicon substrate. Thin Solid Films *516*, 6924–6929, Proceedings on Advanced Materials and Concepts for Photovoltaics EMRS 2007 Conference, Strasbourg, France.

Guo, J., Chen, X., and Wang, C. (2010). Carbon scaffold structured silicon anodes for lithium-ion batteries. J. Mater. Chem. *20*, 5035.

Guo, S., Hu, X., Hou, Y., and Wen, Z. (2017). Tunable synthesis of yolk–shell porous silicon@carbon for optimizing Si/C-based anode of lithium-ion batteries. ACS Appl. Mater. Inter. *9*, 42084–42092.

Hahn, R., Hoeppner, K., Ferch, M., Marquardt, K., Lang, K.D., 2014. Integrated lithium micro batteries for highly miniaturized sensors. In: Energy Self-Sufficient Sensors; 7th GMM-Workshop. Presented at the Energy self-sufficient Sensors; 7th GMM-Workshop, pp. 1–6.

Han, X., Gong, Y., Fu, K., Kelvin), He, X., Hitz, G.T., Dai, J., Pearse, A., Liu, B., Wang, H., et al. (2017). Negating interfacial impedance in garnet-based solid-state Li metal batteries. Nat. Mater. *16*, 572–579.

Harry, K.J., Hallinan, D.T., Parkinson, D.Y., MacDowell, A.A., and Balsara, N.P. (2014). Detection of subsurface structures underneath dendrites formed on cycled lithium metal electrodes. Nat. Mater. *13*, 69–73.

Hoeppner, K., Ferch, M., Froebe, A., Gernhardt, R., Hahn, R., Mackowiak, P., Mukhopadhyay, B., Roder, S., Saalhofen, I., and Lang, K.-D. (2015). Design, fabrication, and testing of silicon-integrated li-ion secondary micro batteries with interdigital electrodes. J. Phys. Conf. Ser. *660*, 012064.

Hu, Y.-S., Demir-Cakan, R., Titirici, M.-M., Müller, J.-O., Schlögl, R., Antonietti, M., and Maier, J. (2008). Superior storage performance of a Si@SiOx/C nanocomposite as anode material for lithium-ion batteries. Angew. Chem. Int. Ed. *47*, 1645–1649.

Ikonen, T., Nissinen, T., Pohjalainen, E., Sorsa, O., Kallio, T., and Lehto, V.-P. (2017). Electrochemically anodized porous silicon: towards simple and affordable anode material for Li-ion batteries. Sci. Rep. *7*, 7880.

Jarvis, K.L., Barnes, T.J., and Prestidge, C.A. (2008). Aqueous and thermal oxidation of porous silicon microparticles: implications on molecular interactions. Langmuir *24*, 14222–14226.

Jia, H., Zheng, J., Song, J., Luo, L., Yi, R., Estevez, L., Zhao, W., Patel, R., Li, X., and Zhang, J.-G. (2018). A novel approach to synthesize micrometer-sized porous silicon as a high performance anode for lithium-ion batteries. Nano Energy *50*, 589–597.

Jiao, S., Zheng, J., Li, Q., Li, X., Engelhard, M.H., Cao, R., Zhang, J.-G., and Xu, W. (2018). Behavior of lithium metal anodes under various capacity utilization and high current density in lithium metal batteries. Joule *2*, 110–124.

Jin, Y., Zhu, B., Lu, Z., Liu, N., and Zhu, J. (2017). Challenges and recent progress in the development of Si anodes for lithium-ion battery. Adv. Energy Mater. *7*, 1700715.

Job, R., Ulyashin, A.G., Fahrner, W.R., Beaufort, M.-F., and Barbot, J.-F. (2003). μ-Raman investigations of plasma hydrogenated silicon. Eur. Phys. J. Appl. Phys. *23*, 25–32.

Karbassian, F. (2018). Porous Silicon. Porosity - Process, Technologies and Applications (InTech Open).

Kim, K.H., Bai, G., Nicolet, M., and Venezia, A. (1991). Strain in porous Si with and without capping layers. J. Appl. Phys. *69*, 2201–2205.

Kumagai, J. (2020). The return of the lithium-metal battery. IEEE Spectr. *57*, 30–31.

Lee, K.-W., Park, D.-K., Kim, Y.-Y., and Shin, H.-J. (2005). Investigation of the interface region between a porous silicon layer and a silicon substrate. Thin Solid Films *478*, 183–187.

Liang, Z., Lin, D., Zhao, J., Lu, Z., Liu, Y., Liu, C., Lu, Y., Wang, H., Yan, K., Tao, X., and Cui, Y. (2016). Composite lithium metal anode by melt infusion of lithium into a 3D conducting scaffold with lithiophilic coating. Proc. Natl. Acad. Sci. U S A *113*, 2862–2867.

Liu, S., Ji, X., Yue, J., Hou, S., Wang, P., Cui, C., Chen, J., Shao, B., Li, J., Han, F., et al. (2020). High interfacial-energy interphase promoting safe lithium metal batteries. J. Am. Chem. Soc. *142*, 2438–2447.

Liu, W., Li, W., Zhuo, D., Zheng, G., Lu, Z., Liu, K., and Cui, Y. (2017). Core–shell nanoparticle coating as an interfacial layer for dendrite-free lithium metal anodes. ACS Cent. Sci. *3*, 135–140.

Lu, D., Shao, Y., Lozano, T., Bennett, W.D., Graff, G.L., Polzin, B., Zhang, J., Engelhard, M.H., Saenz, N.T., Henderson, W.A., et al. (2015a). Failure mechanism for fast-charged lithium metal batteries with liquid electrolytes. Adv. Energy Mater. *5*, 1400993.

Lu, Z., Liu, N., Lee, H.-W., Zhao, J., Li, W., Li, Y., and Cui, Y. (2015). Nonfilling carbon coating of porous silicon micrometer-sized particles for high-performance lithium battery anodes. ACS Nano *9*, 2540–2547.

Marty, O., Nychyporuk, T., de la Torre, J., Lysenko, V., Bremond, G., and Barbier, D. (2006). Straining of monocrystalline silicon thin films with the use of porous silicon as stress generating nanomaterial. Appl. Phys. Lett. *88*, 101909.

Ogata, Y., Niki, H., Sakka, T., and Iwasaki, M. (1995). Oxidation of porous silicon under water vapor environment. J. Electrochem. Soc. *142*, 1595–1601.

Pender, J.P., Jha, G., Youn, D.H., Ziegler, J.M., Andoni, I., Choi, E.J., Heller, A., Dunn, B.S., Weiss, P.S., Penner, R.M., and Mullins, C.B. (2020). Electrode degradation in lithium-ion batteries. ACS Nano *14*, 1243–1295.

Pikul, J.H., and Ning, H. (2018). Powering the internet of things. Joule *2*, 1036–1038.

Schnabel, M., Arca, E., Ha, Y., Stetson, C., Teeter, G., Han, S.-D., and Stradins, P. (2020a). Enhanced interfacial stability of Si anodes for Li-ion batteries via surface SiO2 coating. ACS Appl. Energy Mater. https://doi.org/10.1021/acsaem.0c01337.

Schnabel, M., Harvey, S.P., Arca, E., Stetson, C., Teeter, G., Ban, C., and Stradins, P. (2020b). Surface SiO2 thickness controls uniform-to-localized transition in lithiation of silicon anodes for lithium-ion batteries. ACS Appl. Mater. Inter. *12*, 27017–27028.

Shen, D., Huang, C., Gan, L., Liu, J., Gong, Z., and Long, M. (2018). Rational design of Si@SiO2/C composites using sustainable cellulose as a carbon resource for anodes in lithium-ion batteries. ACS Appl. Mater. Inter. *10*, 7946–7954.

Shen, X., Zhang, R., Chen, X., Cheng, X.-B., Li, X., and Zhang, Q. (2020). The failure of solid electrolyte interphase on Li metal anode: structural uniformity or mechanical strength? Adv. Energy Mater. *10*, 1903645.

Souza, J.P.de, Collins, J., Sadana, D.K., 2020a. Battery Structure with an Anode Structure Containing a Porous Region and Method of Operation. US20200014059A1.

Souza, J.P.de, Collins, J., Sadana, D.K., Bedell, S.W., 2020b. Rechargeable Lithium-Ion Battery with an Anode Structure Containing a Porous Region. US20200014060A1.

Souza, J.P.de, Collins, J., Sadana, D.K., Ott, J.A., Hopstaken, M.J.P., Bedell, S.W., 2020c. Method of Making an Anode Structure Containing a Porous Region. US20200014018A1.

Souza, J.P.de, Sadana, D.K., Collins, J., 2020d. Kinetically Fast Charging Lithium-Ion Battery. US20200014058A1.

Souza, J.P.D., Collins, J., Sadana, D., Bedell, S., Ott, J., Hopstaken, M.J.P., 2020e. Rechargeable Lithium-Ion Battery with an Anode Structure Containing a Porous Region. WO2020008285A1.

Stragier, A.-S., Signamarcheix, T., Salvetat, T., Nolot, E., Dechamp, J., Mercier, D., Gergaud, P., Tauzin, A., Clavelier, L., and Lemiti, M. (2010). 200 mm silicon on porous layer substrates made by the smart cut technology for double layer transfer applications. ECS Trans. *33*, 207.

Su, X., Wu, Q., Li, J., Xiao, X., Lott, A., Lu, W., Sheldon, B.W., and Wu, J. (2014). Silicon-based nanomaterials for lithium-ion batteries: a review. Adv. Energy Mater. *4*, 1300882.

Sugiyama, H., and Nittono, O. (1990). Microstructure and lattice distortion of anodized porous silicon layers. J. Cryst. Growth *103*, 156–163.

Sun, X., Keating, A., Parish, G., 2014. Stress control of porous silicon film for microelectromechanical systems. In: 2014 Conference on Optoelectronic and Microelectronic Materials Devices. Presented at the 2014 Conference on Optoelectronic and Microelectronic Materials Devices, pp. 214–216.

Tang, W., Yin, X., Kang, S., Chen, Z., Tian, B., Teo, S.L., Wang, X., Chi, X., Loh, K.P., Lee, H.-W., and Zheng, G.W. (2018). Lithium silicide surface enrichment: a solution to lithium metal battery. Adv. Mater. *30*, 1801745.

Thevenin, J.G., and Muller, R.H. (1987). Study of the Li/Li3 N electrode in an organic electrolyte. J. Electrochem. Soc. *134*, 2650.

Tsai, C.-L., Roddatis, V., Chandran, C.V., Ma, Q., Uhlenbruck, S., Bram, M., Heitjans, P., and Guillon, O. (2016). Li7La3Zr2O12 interface modification for Li dendrite prevention. ACS Appl. Mater. Inter. *8*, 10617–10626.

Unagami, T. (1980). Formation mechanism of porous silicon layer by anodization in HF solution. J. Electrochem. Soc. *127*, 476.

Volodin, V.A., and Koshelev, D.I. (2013). Quantitative analysis of hydrogen in amorphous silicon using Raman scattering spectroscopy: Infrared and Raman spectroscopy study of a-Si:H films. J. Raman Spectrosc. *44*, 1760–1764.

Vrankovic, D., Graczyk-Zajac, M., Kalcher, C., Rohrer, J., Becker, M., Stabler, C., Trykowski, G., Albe, K., and Riedel, R. (2017). Highly porous silicon embedded in a ceramic matrix: a stable high-capacity electrode for Li-ion batteries. ACS Nano *11*, 11409–11416.

Wang, C., Wu, H., Chen, Z., McDowell, M.T., Cui, Y., and Bao, Z. (2013). Self-healing chemistry enables the stable operation of silicon microparticle anodes for high-energy lithium-ion batteries. Nat. Chem. *5*, 1042–1048.

Wu, B., Wang, S., Lochala, J., Desrochers, D., Liu, B., Zhang, W., Yang, J., and Xiao, J. (2018). The role of the solid electrolyte interphase layer in preventing Li dendrite growth in solid-state batteries. Energy Environ. Sci. *11*, 1803–1810.

Xiao, Q., Gu, M., Yang, H., Li, B., Zhang, C., Liu, Y., Liu, F., Dai, F., Yang, L., Liu, Z., et al. (2015). Inward lithium-ion breathing of hierarchically porous silicon anodes. Nat. Commun. *6*, 8844.

Xing, Y., Shen, T., Guo, T., Wang, X., Xia, X., Gu, C., and Tu, J. (2018). A novel durable double-conductive core-shell structure applying to the synthesis of silicon anode for lithium ion batteries. J. Power Sources *384*, 207–213.

Xu, Z., Yang, J., Zhang, T., Nuli, Y., Wang, J., and Hirano, S. (2018). Silicon microparticle anodes with self-healing multiple network binder. Joule *2*, 950–961.

Yan, C., Yao, Y.-X., Chen, X., Cheng, X.-B., Zhang, X.-Q., Huang, J.-Q., and Zhang, Q. (2018). Lithium nitrate solvation chemistry in carbonate electrolyte sustains high-voltage lithium metal batteries. Angew. Chem. Int. Ed. *57*, 14055–14059.

Yan, K., Lu, Z., Lee, H.-W., Xiong, F., Hsu, P.-C., Li, Y., Zhao, J., Chu, S., and Cui, Y. (2016). Selective deposition and stable encapsulation of lithium through heterogeneous seeded growth. Nat. Energy *1*, 16010.

Yang, C.-P., Yin, Y.-X., Zhang, S.-F., Li, N.-W., and Guo, Y.-G. (2015). Accommodating lithium into 3D current collectors with a submicron skeleton towards long-life lithium metal anodes. Nat. Commun. *6*, 8058.

Zhai, W., Ai, Q., Chen, L., Wei, S., Li, D., Zhang, L., Si, P., Feng, J., and Ci, L. (2017). Walnut-inspired microsized porous silicon/graphene core–shell composites for high-performance lithium-ion battery anodes. Nano Res. *10*, 4274–4283.

Zhang, D.-X., Yoshikawa, C., Welch, N.G., Pasic, P., Thissen, H., and Voelcker, N.H. (2019). Spatially controlled surface modification of porous silicon for sustained drug delivery applications. Sci. Rep. *9*, 1367.

Zhang, Huimin, Liao, X., Guan, Y., Xiang, Y., Li, M., Zhang, W., Zhu, X., Ming, H., Lu, L., Qiu, J., et al. (2018). Lithiophilic-lithiophobic gradient interfacial layer for a highly stable lithium metal anode. Nat. Commun. *9*, 3729.

Zhou, XiaoHui, Huang, W., Shi, C., Wang, K., Zhang, R., Guo, J., Wen, Y., Zhang, S., Wang, Q., Huang, L., et al. (2018). Enabling lithium-metal anode encapsulated in a 3D carbon skeleton with a superior rate performance and capacity retention in full cells. ACS Appl. Mater. Inter. *10*, 35296–35305.

iScience, Volume *23*

Supplemental Information

Diffusion-Controlled Porous Crystalline Silicon Lithium Metal Batteries

John Collins, Joel P. de Souza, Marinus Hopstaken, John A. Ott, Stephen W. Bedell, and Devendra K. Sadana

Supporting Data Figures

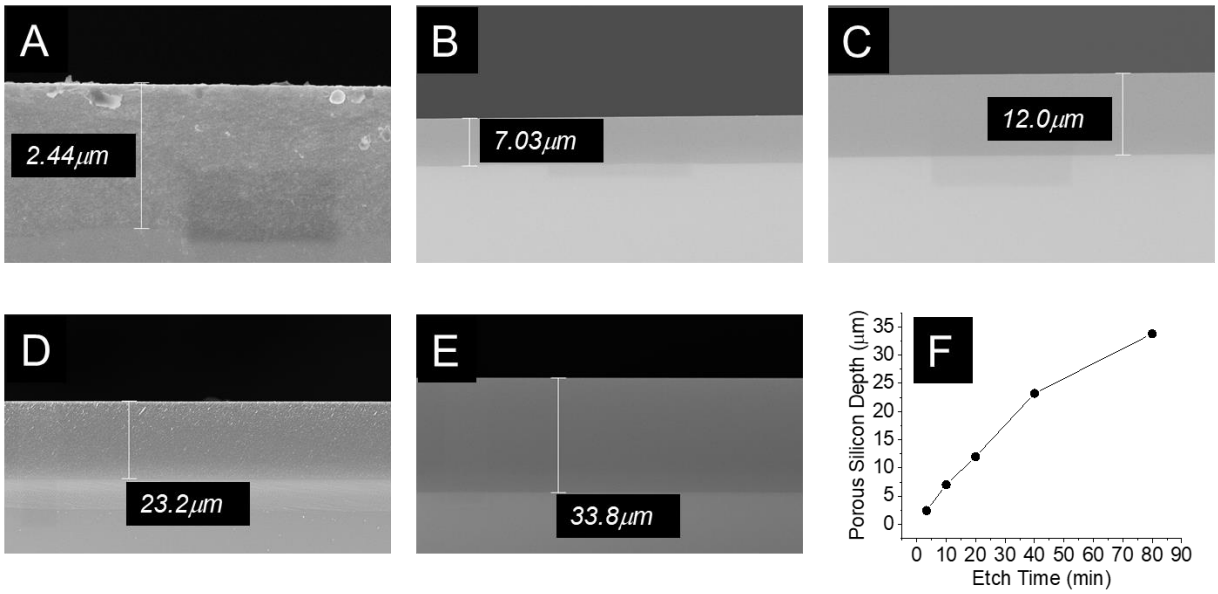

Figure S1. The impact of SC-PCS thickness as a function of anodization time, related to Figure 1. Scanning electron micrographs (SEM) cross sections of p^+ substrates etched for: (A) 200s (B) 600s (C) 1200s (D) 2400s (E) 4800s. (F) Plot of the depth of porous silicon integrated into wafer as a function of anodization etch time.

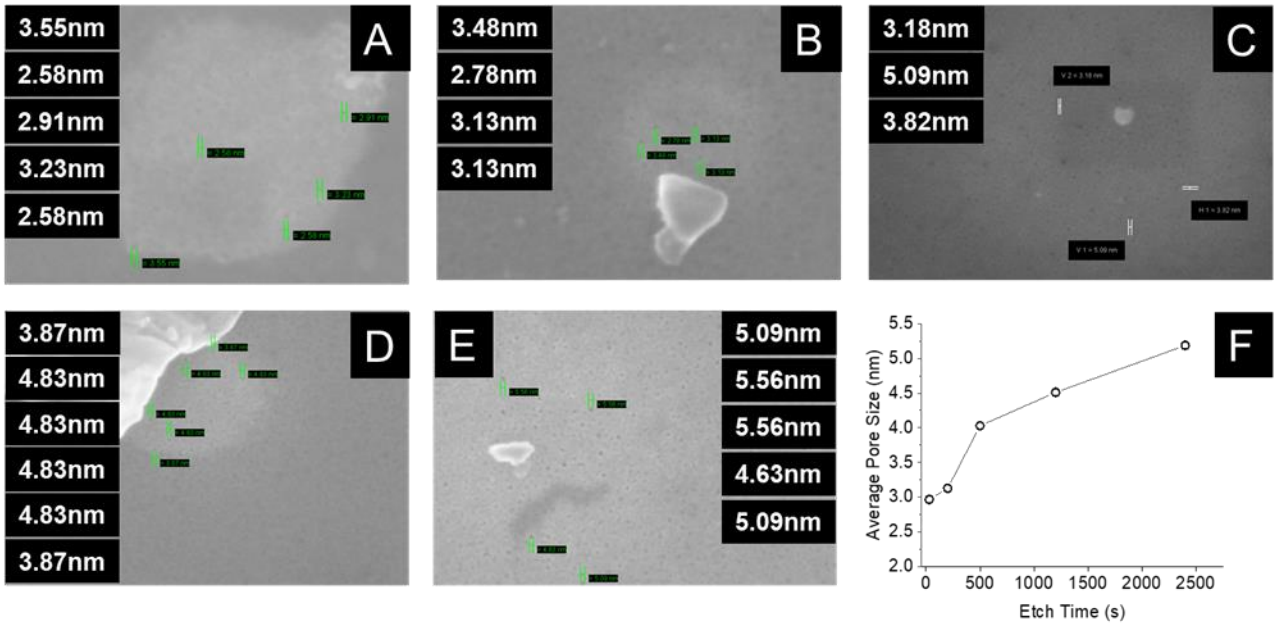

Figure S2. The impact of anodization time on pore diameter of SC-PCS, related to Figure 1. Top-down SEM micrographs of (A) 30s (B) 200s (C) 500s (D) 1200s (E) 2400s. Values indicate pore diameters measured for each SEM. (F) The average pore size as a function of anodization etching time.

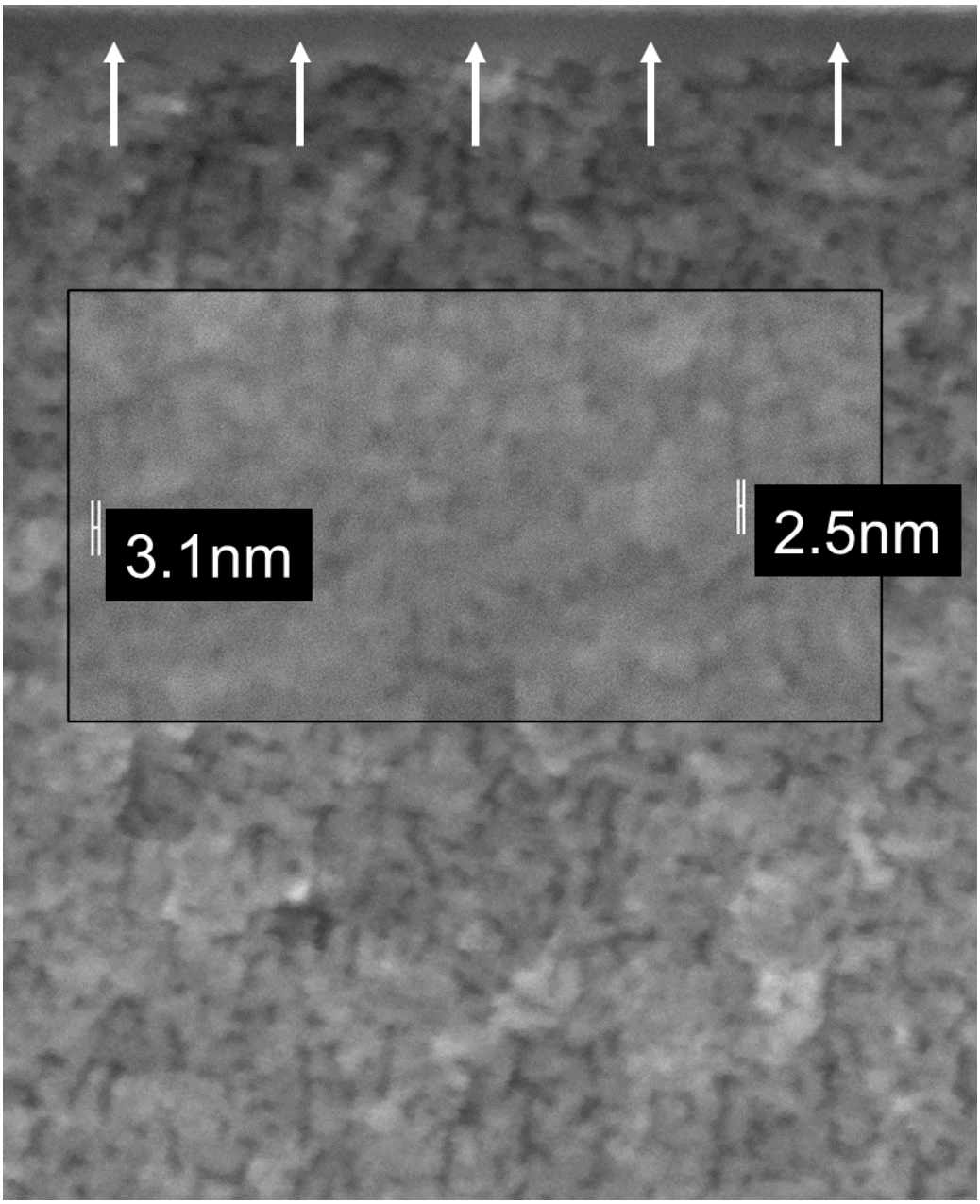

Figure S3. The effect of the top denuded PCS layer in creating low-strain smaller diameter nanoporosity deep into the silicon wafer bulk upon anodization, related to Figure 2 and Table 1. SEM cross section displaying the denuded SC-PCS layer, which resides on the top-most ~30nm of the surface of the silicon wafer (white arrows), containing a highly crystalline composition with low strain (Table 1) resulting from the removal of non-silicon heteromaterial by pre-anodization surface treatment. The inset displays a high magnification SEM cross section revealing the low-strain, high crystalline properties of the denuded layer that are communicated throughout the etched portion of the substrate, upon anodization, as evidenced by the presence of smaller average diameter nanopores deep in the SC-PCS bulk.

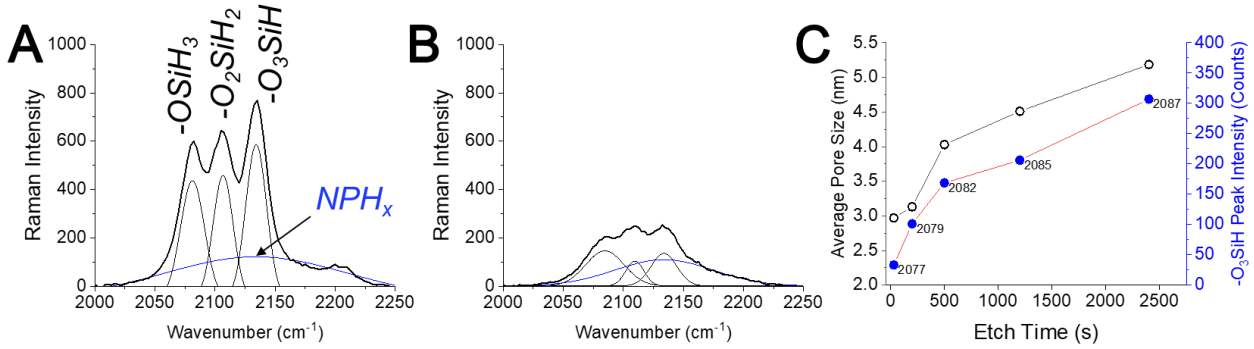

Figure S4. Deconvolution of SC and NSC anodized porous silicon, related to Figure 3. Raman spectra of (A) 1200s NSC-PS (B) 1200s SC-PCS. Peak assignments are indicated. (C) Average pore size and -O_3Si—H Raman vibration frequency for SC-PCS samples anodized up to 2400s. O_3Si—H vibration frequencies (cm^{-1}) are indicated with each peak intensity data point.

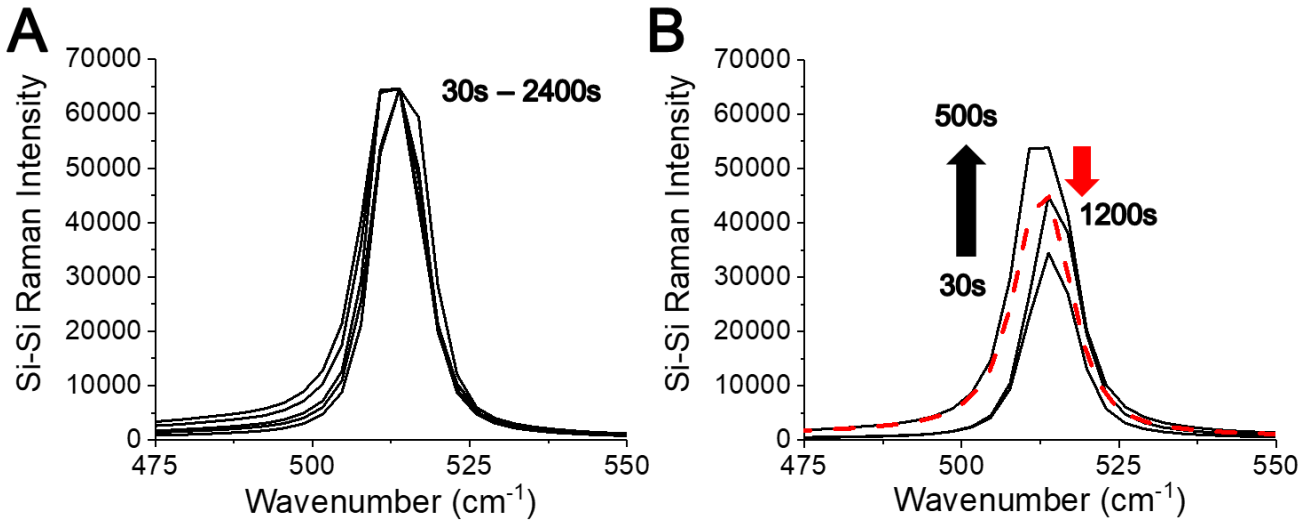

Figure S5. The impact of pre-anodization surface cleaning treatment on denuded silicon crystallinity, related to Figure 2 and Figure 3. (A) NSC-PS up to 1200s (dashed line) of anodization time (B) SC-PCS up to 2400s of anodization time.

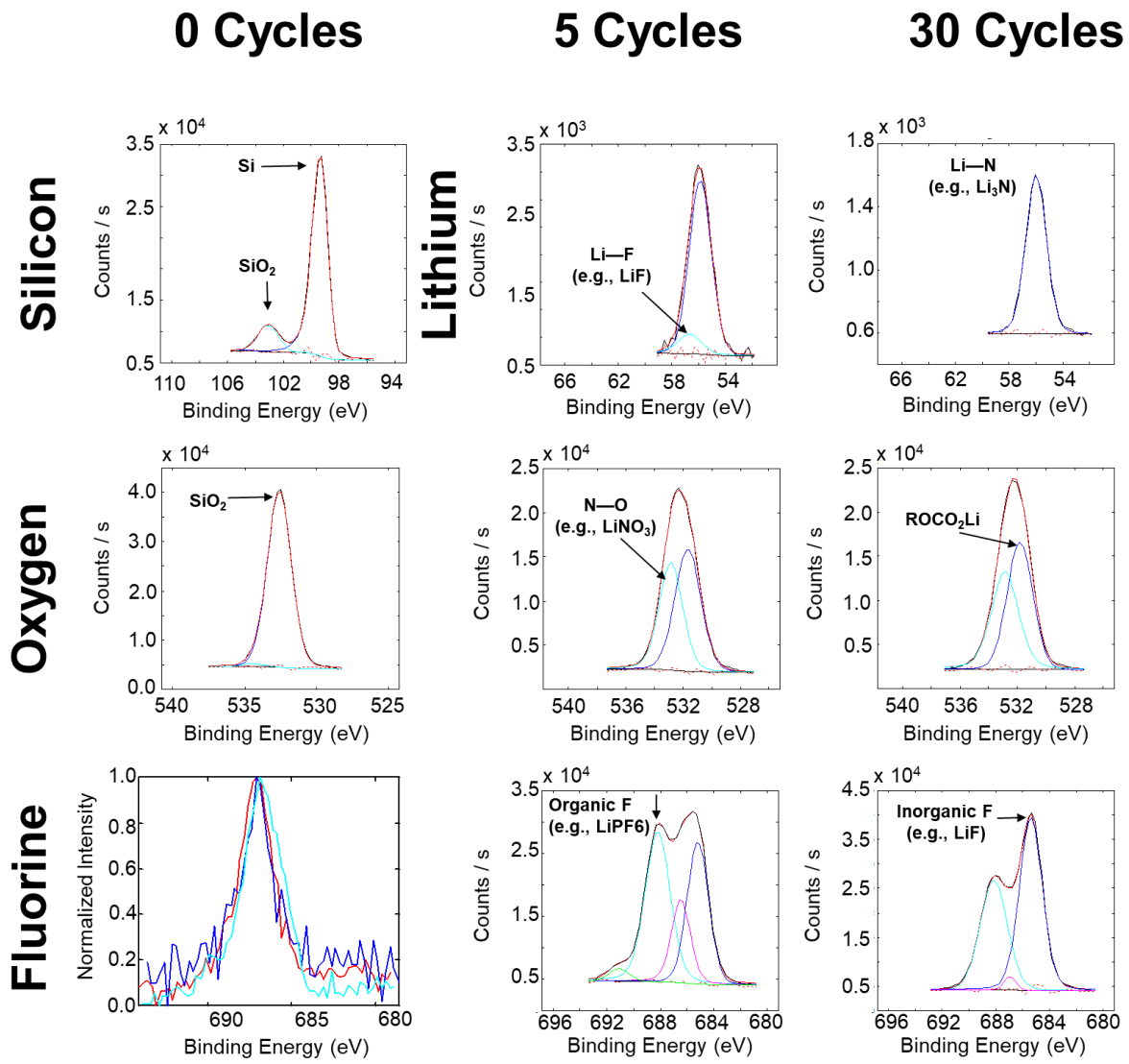

Figure S6. X-ray Photoelectron Spectra (XPS) and deconvoluted peak fitting of 200s anodized SC-PCS anode at different cycling stages, related to Figure 5 and 6. Cycling number and element are indicated for each spectrum with specific bonding or specie designations labeled. Multiple normalized intensity scans of fluorine at 0 cycles are shown to indicate reproducibility of composition at different wafer areas.

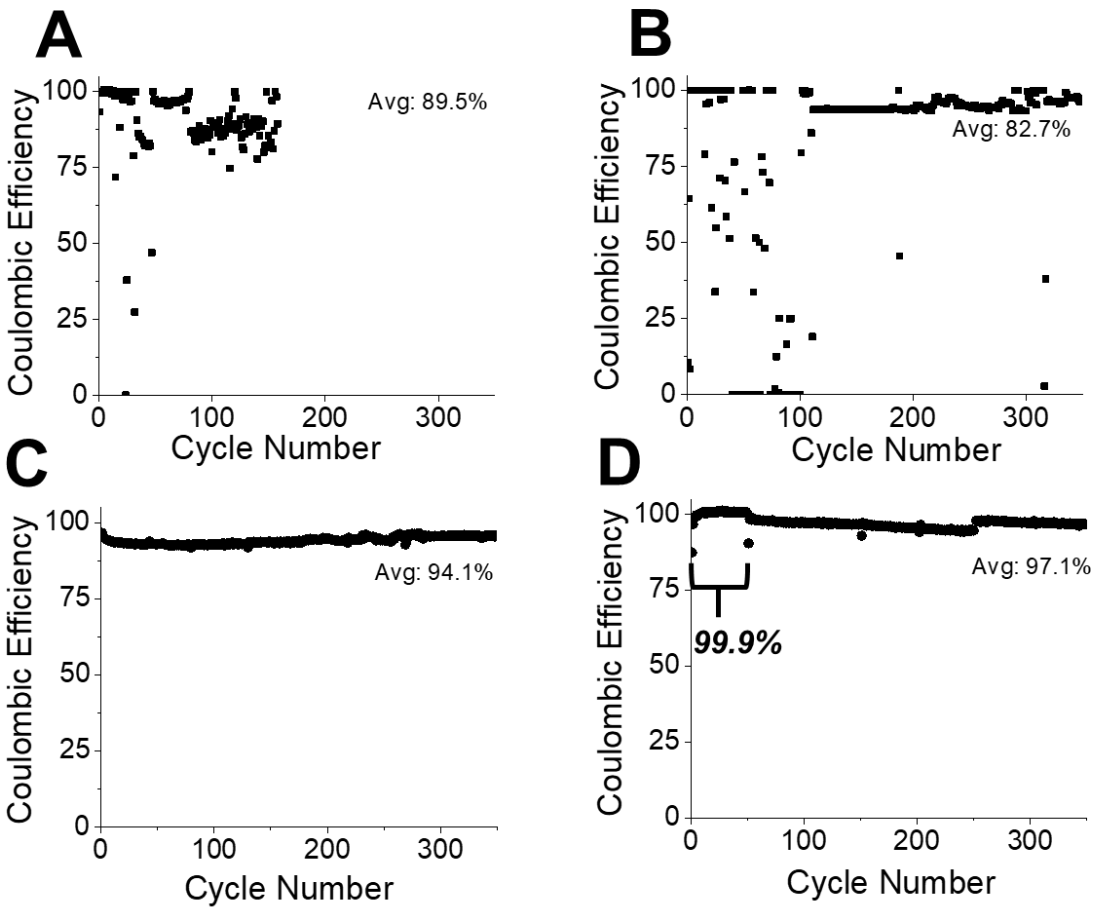

Figure S7. Coulombic efficiency of non-pre-lithiated and pre-lithiated full cells, related to Figure 12. 160μm LCO containing full cells containing (A) 200s and (B) 500s SC-PCS. Electrochemical pre-lithiated SC-PCS full cells with (C) 160μm LCO / 500s SC-PCS anode and (D) 100μm NMC / 80 min SC-PCS with nickel protected wafer backside. Average % coulombic efficiency is displayed for each cell. Coulombic efficiency for non-pre-lithiated cells were calculated by dividing discharge/charge in coulombs during initial cycles. Upon sufficient lithiation and migration of denuded region within the porous silicon, subsequent coulombic efficiency was calculated by dividing charge/discharge in coulombs. Pre-lithiated cells utilized coulombs during charge + average coulombs during charge saturation hold time / discharge in coulombs.

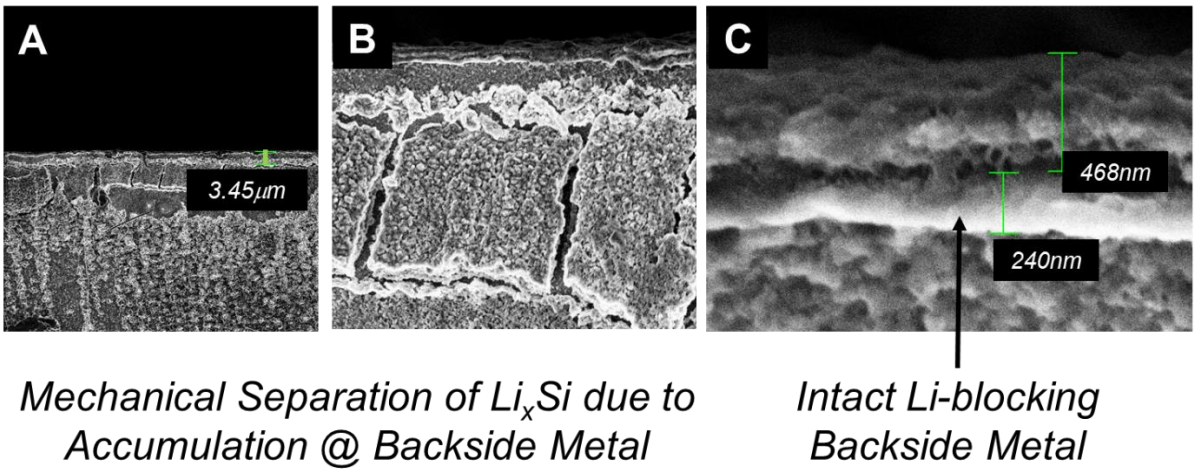

Figure S8. The prevention of substrate degradation with nickel metal encapsulation of the SC-PCS silicon substrate backside, related to Figure 12D. (A) Low magnification SEM cross section displaying aggregated, concentrated and mechanically separate (B) Cracking at the wafer backside due to accumulation of Li_xSi species at (C) Li-blocking metal (240nm) encapsulation layer.

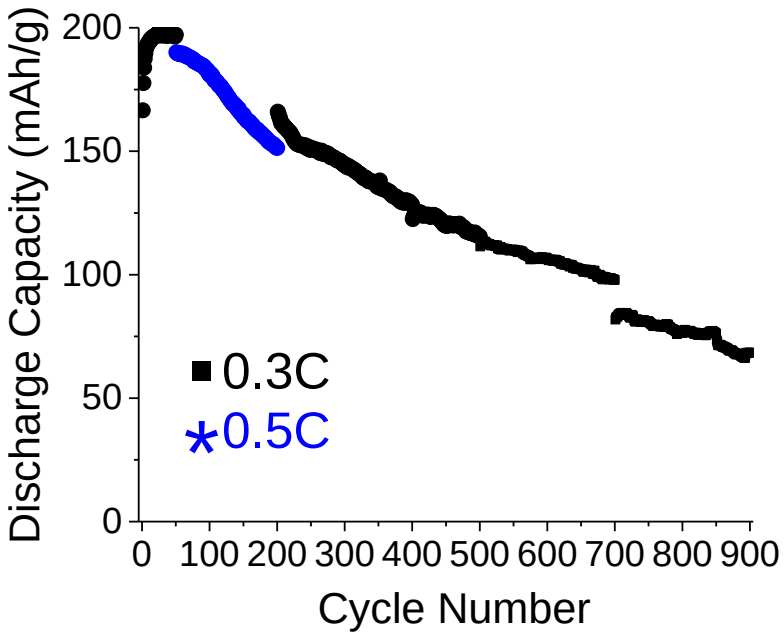

Figure S9. The initial 900 cycles of the pre-lithiated NMC811 / 80 min SC-PCS full cell, related to Figure 13D. Relative rates of discharge are displayed. Average capacity over 900 cycles was 125mAh/g.

Transparent Methods

Porous Silicon Pre/post-anodization Organic Particle Cleaning. p^+ wafers with high boron-doping (~1E19) were utilized for all porous silicon anodes. Standard Clean 1, (SC-1) was first used to remove organic particulates from the substrates prior to anodization, wafers were immersed in a stirred solution of 1:1:5 ratio of NH_4OH, H_2O_2 and H_2O at an elevated temperature (e.g., >30C), and then rinsed with deionized water and dried with nitrogen gas. After anodization, a second clean sequence was utilized where the wafer sample was: A) boiled in acetone for 10min B) boiled in methanol for 10min C) immersed in isopropyl alcohol for 5min and D) Nitrogen jet dried. Anodized porous silicon samples with organic particle cleaning treatment are herein referred to standard cleaned porous crystalline silicon (SC-PCS), whereas non-cleaned anodized porous silicon samples are referred to as non-standard cleaned porous silicon (NSC-PS).

Anodization. SC-PCS and NSC-PC were anodized by mounting the wafer in an electrochemical Teflon cell that exposes only the polished side of the wafer sample to concentrated hydrofluoric acid (HF). A platinum anode was constructed in the Teflon cell such that a constant proximity and circular distribution could be maintained in solution. All samples were anodized using the same constant current density of a few mA/cm^2 for a given anodization time. The sample was removed from the electrochemical cell and rinsed with DI water for 1min followed by nitrogen jet drying. Wafer samples were then diamond cut to obtain the desired diameter size: 15.5mm for non-pre-lithiated cells and 13.5mm for pre-lithiated cells.

Cathode Synthesis. 160 micron thick lithium cobalt oxide (LCO) and 100 micron nickel manganese cobalt (NMC811) electrodes contained a composition of 90% active material, 5% PVDF binder and 5% carbon black. For example: 0.90g Active material, 0.05 g PVDF and 0.05 g carbon black with total 7 grams of NMP were mixed with zirconia balls for 1-5 minutes at 2000 rpm in a mixer at room temperature to get slurry consistent for casting. The slurry was casted on Aluminum foil (16 um) and doctor bladed at desired thickness after evaporation of NMP at 100 C for several hours in a dry air circulated oven. The NMC811 cathodes displayed areal capacities of $1.5mAh/cm^2$ with mass loading of $7.6mg/cm^2$ and a density of $0.70g/cm^3$. The experimental areal capacity of the pre-lithiated SC-PCS anodes was determined to be ~$2.5mAh/cm^2$, yielding a full cell n/p ration of 1.7 / 1.

Electrochemical Pre-lithiation. Cleaned and anodized porous silicon substrates were immersed with liquid electrolyte, an electrolyte-soaked separator followed by a lithium metal foil disk and sealed in a Swagelok cell. Cells were pre-lithiated at a 0.01C rate for 8hrs (for LCO containing full cells) or 10hrs (for NMC containing full cells), or until 0.025V was achieved.

Full Cell Assembly. Full cells were assembled with a 1M LiPF6 in EC:DMC:DEC (1:1:1) volume ratio electrolyte purchased from NEI Corporation. Crimped 2032 coin cells were used for encapsulation with arrangement of components in the following order: aluminum coated coin cell base, cathode, separator, porous silicon anode, stainless steel spacer, spring and coin cell cap.

Dynamic SIMS. SIMS depth profiles were acquired using a magnetic sector instrument (Cameca Wf), employing 2 keV primary Cs^+ ion beam (rastered over 225μ). Different secondary Cs_nM^+ cluster ions were detected, depending on species (e.g. atmospherics M= H, C, O, F detected as Cs_2M^+; Li detected as $CsLi^+$).

Electrochemical Testing. Coin cells were cycling using a multichannel Arbin battery testing tool in galvanostatic mode at indicated C-rates. Charge saturation 4.2V hold was utilized for pre-lithiated cells until current dropped to 25% of applied charge current. NMC containing cells were cycled between 2.7V to 4.2V whereas LCO containing cells were cycled between 3.0V and 4.2V. Electrochemical impedance spectroscopy (EIS) was conducted on tested coin cells using a Parstat 4000 potentiostat using with a 10mV excitation amplitude over a 1MHz to 199mHz frequency range conducted at 0V applied bias upon cell discharge. Cells were given enough time for equilibrium voltages to obtain less than 500uV of voltage drift prior to conducting EIS measurements. Resistance values were estimated from the diameter of semi-circle fits using Z-View software. Total energy density of discharge was calculated by adding the products of the instantaneous voltage and the current for each time point ($V_t * I_t * dt$) in the discharge curve and

dividing by the mass of the active cathode. Average energy density of the NMC | 4800s SC-PCS full cell was calculated by taking the averages from discharge cycles (1, 2, 20 and 300) shown in Figure 11.

Raman. Raman spectra were acquired on a Horiba Jobin Yvon Aramis confocal Raman microscope using a laser at 532nm, with a 100x objective and theoretical spot size of 0.72 m (diameter = 1.22 λ / NA (where λ is the wavelength of the laser, and NA is the numerical aperture of the microscope objective being used), using 10s acquisition time averaged for 5 scans.

X-Ray Diffraction and X-Ray Reflection. X-ray spectra were acquired on a Philips X'Pert Pro with a 4-bounce Ge monochromator and a PIXcel 1D detector. X-ray reflectivity (XRR) was used to measure the density of the porous films directly from the critical angle, as described with Asgharizadeh, et. al.(Asgharizadeh et al., 2009) Porosity (%) was calculated by the following equation: $(1-(\rho_x/\rho_0))*100$ where ρ_x is the SC-PCS density at anodization time x and ρ_0 is the density of the non-anodized SC crystalline silicon wafer. (004) X-Ray diffraction (XRD) peaks were obtained with a Cu-Kα source (1.54 Å) and generator output of 45kV. In-plane strain was calculated as follows: 1) the angular separation between the 004 bulk Si and porous Si peaks was measured, this is a direct measurement of the perpendicular lattice spacing of the porous Si using the Bragg equation 2) It was assumed that the in-plane lattice parameter of the porous Si remains that of bulk Si (5.43105 A) and that the Poisson ratio is that of Si (0.28). The in-plane and out of plane (perpendicular) lattice parameters were utilized to calculate the equilibrium lattice parameter (the magnitude if it was a cube instead of a rectangular parallelepiped). The difference between the equilibrium lattice parameter, and actual in-plane parameter (which we assume is that of bulk Si) is the in-plane strain values reported.

X-Ray Photoelectron Spectroscopy. XPS spectra were obtained using a PHI5500 with mono-chromated Al-Kα radiation (400W source) with analytical conditions: take-off angle 22deg. and 59eV pass energy). Surface compositional analysis using XPS spectra was performed using CASA XPS v.2.3.

Imaging and Elemental Analysis. Scanning electron micrographs (SEM) were obtained using a Zeiss Leo 1560 SEM with acceleration voltages between 3 to 5kV at working distances between 3 to 5 mm. Transmission electron micrographs (TEM) were acquired on a 300kV JEOL FE TEM, using an EMISPEC EDS system. For both SEM-EDS and TEM-EDS, samples were prepared using a FEI Helios dual beam focused ion beam (FIB), using low energy finish polishing techniques.

Supplemental References

Asgharizadeh, S., Sutton, M., Robbie, K., Brown, T., 2009. X-ray reflectometry characterization of porous silicon films prepared by a glancing-angle deposition method. Phys. Rev. B 79, 125405.